Check for updates

Analysis of metallogenic material sources and metallogenic epoch of the Xiahulin lead-zinc deposit in inner Mongolia, China

Mingxin Duan[1,2,3], Guihu Chen[1,3]*, Tao Liu[1,3], Liye Liu[1,3]* and Xidong Zhao[1,3]

[1]Harbin Center for Integrated Natural Resources Survey, China Geological Survey, Harbin, China, [2]The Northeast Geological Science and Technology Innovation Center of the China Geological Survey, Shenyang, China, [3]Observation and Research Station of Earth Critical Zone in Black Soil, Ministry of Natural Resources, Harbin, China

The Xiahulin lead-zinc deposit serves as a classic skarn-type deposit in the Erguna Block of the Greater Khingan Range, containing uncertain metallogenic sources and epochs. The orebodies form complex shapes in the contact zone between granite and Sinian Ergunahe Formation rocks, with alteration zones characterized by skarnization and silicification, extending 1–5 m from the ore veins. The ores primarily comprise sphalerite, galena, chalcopyrite, pyrite, and quartz, with nested to disseminated structures. Mineralization occurs in four stages: pre-ore, early, main, and post-ore. Geochemical analyses revealed that the sphalerite in the main stage closely resembled syenogranite in trace elements. Sulfur isotopes ($\delta^{34}S$V-CDT = 3.46‰ − 5.96‰) indicated the magmatic sulfur origins, while led isotopes ($^{208}Pb/^{204}Pb$ = 38.188 − 38.214, $^{207}Pb/^{204}Pb$ = 15.591 − 15.599, $^{206}Pb/^{204}Pb$ = 18.437 − 18.442) suggested a mantle-crust mixed source. Zircon Hf isotopes ($^{176}Hf/^{177}Hf$ = 0.282628 − 0.282846) and two-stage model ages (804 − 1309 Ma) indicated the partial melting of newly formed crustal material with minor contamination from ancient crust. The U-Pb dating of syenogranite zircons provided a diagenetic age of 203.8 ± 2.2 Ma. Based on geological and elemental evidence, Xiahulin mineralization likely occurred in the Early Jurassic, originating from the crust-mantle mixtures related to the Mongol-Okhotsk Ocean subduction, marking a period of notable mineralization in the Erguna Block.

1 Introduction

The Erguna Block is located in the eastern segment of the Xingmeng orogenic belt within the Central Asian Orogenic Belt and serves as a notable region for lead-zinc (silver) and copper-molybdenum mineralization. Prospecting activities have identified numerous large-scale deposits, including the Jiawula, Erentaolegai, Biliyagu, and Deerbuer lead-zinc (silver) deposits (Xu, 2020; Jia et al., 2012; Zhu et al., 1999; Sun, 1995; Zhang et al., 2002), as well as the Wunugetushan, Taipingchuan, and Baguanzhong copper-molybdenum deposits (Zhang et al., 2022; Cao, 2020; Hou, 2014). This area's significant lead-zinc and copper-molybdenum resources have attracted considerable attention (Qin et al., 1999; Mao et al.,

2005; Pirajno, 2009; Catchpole et al., 2015). The lead-zinc deposits were primarily identified along the NNE-trending Delbugan fault as veins within the Mesozoic volcanic rocks. Varied conclusions have been drawn regarding the source of the ore-forming materials, such as crust mantle mixed source (Jia et al., 2012; Zhu et al., 1999; Sun, 1995), crust mantle mixed source dominated by mantle source (Li et al., 2011; Zhao et al., 2017), and upper crust (Li et al., 2014). Moreover, their mineralization and ore controlling elements are poorly understood. However, research on skarn-type lead-zinc deposits, such as the Xiahulin deposit, remains limited, with unresolved questions regarding the sources of metallogenic materials and the precise ages of rock formation and mineralization. It is unclear whether there is any correlation between the skarn type lead-zinc deposit and the porphyry type copper molybdenum deposit.

To address these issues, this study investigated the Xiahulin lead-zinc deposit through detailed field geological surveys, petrographic and mineralogical analysis, geochemical studies of ore-forming rocks, trace element composition of sphalerite, and *in-situ* S-Pb isotope composition of the ore to trace the sources of metallogenic materials. Additionally, by analyzing the trace element signatures of the ore-forming rocks and sphalerite and determining the zircon U-Pb age of the ore-forming rocks, we established constraints on the ages of rock formation and mineralization. And through comparative research with typical copper molybdenum deposits in the region, explore the correlation between their formation and evolution process and copper molybdenum deposits such as Badaguan. Furthermore, it is expected to provide new evidence for the large-scale mineralization and tectonic evolution of the Erguna block in the Mesozoic era.

2 Geological background

The Xiahulin lead-zinc deposit is situated in the eastern CAOB, within the eastern segment of the Xingmeng orogenic belt, and in the center of the Erguna Block. The Erguna block borders the Mongolia-Okhotsk suture zone to the northwest and the Xing'an block to the southeast, separated by the Taylor-Xiguitu belt. Geological data indicated that this region developed within the Paleo-Asian Ocean tectonic domain from the Late Proterozoic to the Early Paleozoic, forming the Erguna orogenic belt with a trench-arc-basin system. During the Early to Middle Mesozoic, under the influence of Pacific and Mongolia-Okhotsk tectonic movements, the area underwent oceanic basin subduction and collisional orogenesis, resulting in porphyry-type deposits such as Baguanzhong, Babayi, and Taipingchuan. From the Middle to Late Mesozoic, the region evolved through stages of continental rifting, yielding rich deposits of lead, zinc, silver, and other minerals.

The exposed strata in the region span from the Precambrian through the Paleozoic to the Meso-Cenozoic, with the basement mainly composed of the Jiageda Formation (Nhj) and the Ergunahe Formation (Ze), whereas the overlying strata consist primarily of the Paleozoic Hongshuiquan Formation (C_1h) and Mesozoic volcanic rocks. The metamorphic and carbonate rocks of the Jiageda Formation (Nhj) and Ergunahe Formation (Ze) serve as host strata for the lead-zinc and gold deposits. Due to their similarities to the stratigraphy and rock assemblages of the Bayan Obo rare earth deposit, they are

prime targets for evaluating strategic minerals, including "three rare" elements. The Mesozoic Tamulangou Formation (J_2t), Manketouebo Formation (J_3mk), and Manitu Formation (J_3mn) host numerous hydrothermal vein-type lead-zinc-silver deposits distributed along the Delbugan fault, exhibiting significant metallogenic potential. The strata exposed in the mining area primarily include the Proterozoic Sinian Ergunahe Formation (Ze) marble, quartzite, schist, and Middle Jurassic Tamulangou Formation (J_2t), with terrigenous clastic rocks, andesite, andesitic basalt, and intermediate-basic volcaniclastic rocks (Figure 1C). Notably, the contact zone between the Ergunahe Formation (Ze) marble and intrusive rocks is characterized by extensive skarn alteration, presenting a favorable zone for mineralization.

The intrusive rocks in the mining area are primarily composed of Early Yanshanian granite, Hercynian granite porphyry, and Caledonian biotite granite with dike rocks. Notably, the Early Yanshanian medium-grained potassium feldspar granite, located in the outer contact zone with quartzite and marble, exhibits extensive skarn alteration in the surrounding rocks.

Regional structures primarily consist of fault and fold structures. The fault structures are categorized into three groups: NNE-trending concealed faults, which are pre-mineralization structures; near-EW (NWW)-trending fracture zones, which formed during mineralization; and near-NS-trending faults, which are post-mineralization structures. The mining area lies on the northwest wing of the Shanghulin anticline, with strata generally forming a slightly undulating monoclinic structure that trends NE and dips NW at an angle of approximately 10°–30°.

3 Ore deposit geology

The orebodies in the Xiahulin mining area exhibit complex forms, including pillars, pods, lenticular bodies, and lenses (Figure 2), with two main orebodies: Orebody I and Orebody II. Primary ore structures range from nested to disseminated, with massive structures occurring less frequently. The ore textures included metasomatic dissolution (Figure 3A), solid solution unmixing (Figure 3B), and anhedral granular textures (Figure 3C).

Sphalerite and galena are the primary ore minerals, with pyrite and chalcopyrite as the secondary minerals. Magnetite (Figure 3B) and hematite are also prevalent. The gangue minerals consist of garnet, quartz, calcite, chlorite (Figure 3E), sericite (Figure 3F), trace amounts of fluorite (Figure 3D), and cassiterite.

The orebodies are located in the contact zone between the Early Yanshanian granite and Sinian Ergunahe Formation quartzite and marble. The wall rocks consist of skarnized marble and skarn, with no intercalations within the orebodies. Wall-rock mineralization and alteration primarily include skarnization, silicification, chloritization, sericitization, fluoritization, and carbonatization.

Based on mineral paragenesis, intergrowth relationships, and wall-rock alterations, the mineralization stages of the Xiahulin deposit are classified into skarn and quartz-sulfide stages. The skarn stage comprises the skarn substage (garnet, diopside, tremolite, epidote, and actinolite) and the oxide substage (magnetite, hematite, and quartz). The quartz-sulfide stage is further divided into the early sulfide stage (colloform pyrite and chalcopyrite with minor sphalerite and galena), the late sulfide stage (main mineralization
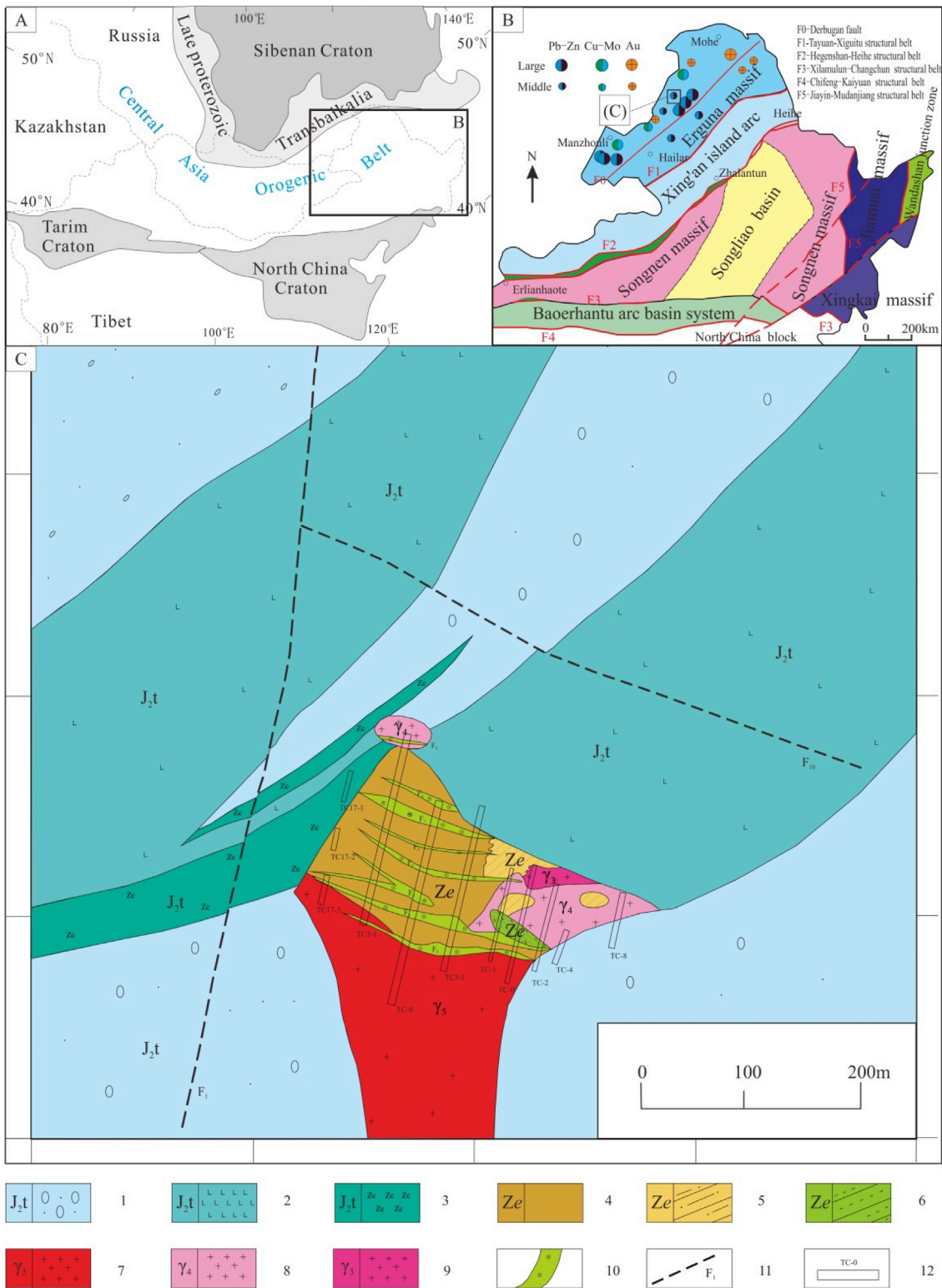
FIGURE 1
Geotectonic location map [(A) after Jahn et al., 2004; (B) modified by Pan et al., 2009] and geological map [(C) modified by Wang et al., 2003] of the Xiahulin deposit. 1-Terrigenous clastic rocks of the Tamulangou Formation; 2- Andesite and basaltic andesite of the Tamulangou Formation; 3- Intermediate-basic volcaniclastic rocks of the Tamulangou For-mation; 4- Dolomitic marble of the Ergunahe Formation; 5- Quartzite of the Ergunahe For-mation; 6- Chlorite schist of the Ergunahe Formation; 7- Monzogranite of the Early Yanshanian period; 8- Granitic porphyry of the Hercynian period; 9- Biotite granite of the Caledonian period; 10- Silicified.
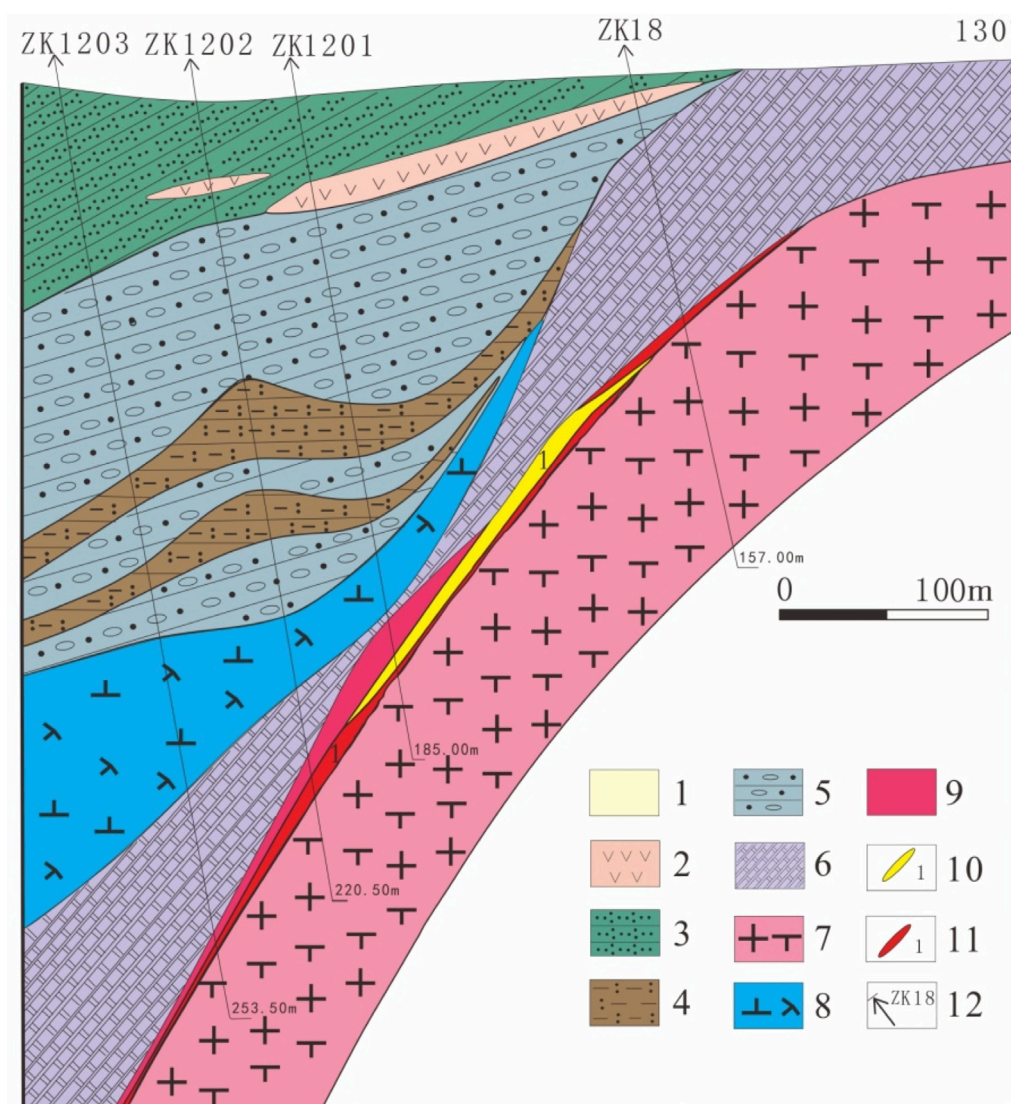
FIGURE 2
Combined Sectional Map of Exploration Line No. 12 of the Xiahulin Lead-Zinc Mine (Revised Based on Xu et al., 2017). 1- Quaternary deposits; 2- Intermediate-basic volcanic rocks of the Tamulangou Formation; 3- Tuffaceous sandstone of the Tamulangou Formation; 4- Argillaceous siltstone of the Wanbao Formation; 5- Glauconitic sandstone of the Wanbao Formation; 6- Marble of the Ergunahe For-mation; 7- K-feldspar granite; 8- Diorite porphyry; 9- Tectonic breccia; 10- Silver orebodies and their numbers; 11- Lead-zinc orebodies and their numbers; 12- Drill holes and their numbers.

phase with pyrite, sphalerite, chalcopyrite, and galena), and the quartz-calcite stage (with minor pyrite).

4 Sample characteristics and analytical methods

4.1 Major, rare earth, and trace elements

To investigate the relationship between syenogranite and mineralization in the Xiahulin lead-zinc deposit, samples from the orebody and contact zone near the 90-meter adit of the No. 3 inclined shaft were collected for trace element and REE analysis in sphalerite, as well as for major element, REE, and trace element analysis in

syenogranite (Section 4.3). The sample preparation and testing were conducted at the Analytical Laboratory of the Harbin Comprehensive Survey Center. The AXIOSMAX X-ray fluorescence spectrometer from Malvern Paralytical was utilized to measure the concentration of primary elements in the samples, employing the instru-ment's quantitative analysis software. The major elements were analyzed by XRF with an accuracy of 97%–98%. The sample is pre crushed to 200 mesh, dried at 105°C for 2 h, taken out and cooled to room temperature in a dryer. Accurately weigh (0.5 ± 0.0002) g of the sample and (5 ± 0.0005) g of the mixed flux $(Li_2B_4O_7\text{-}LiBO_2)$ on an analytical balance and place them in a porcelain crucible. Stir evenly and transfer the mixed sample into a platinum crucible (95% Pt+5% Au). Use a dropper with a rubber tip to add 300 g/L NH4NO₃ solution and 5 drops of 200 g/L NH_4Br solution. Place the platinum crucible into the
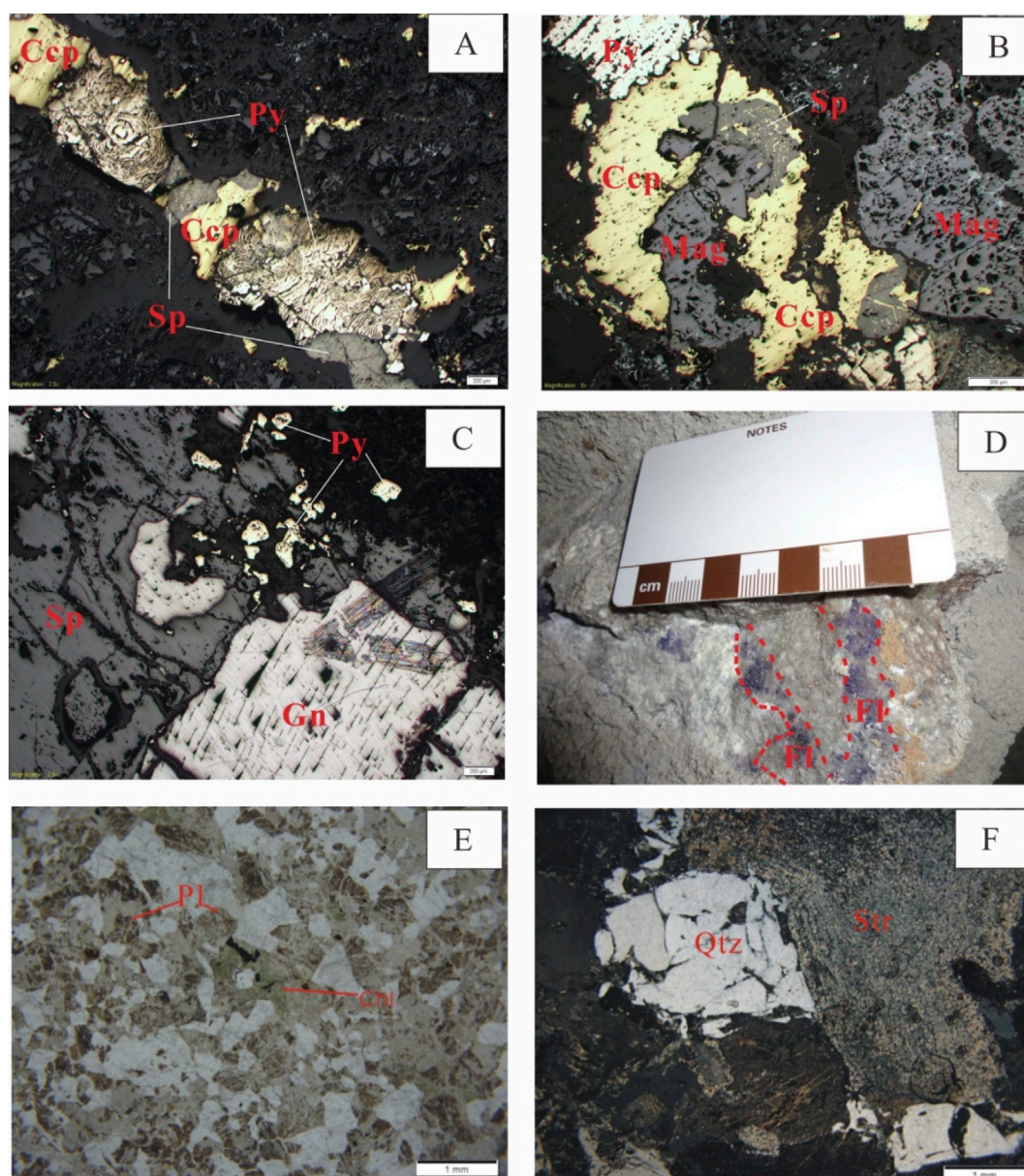
FIGURE 3
Photographs of Specimens, Polished Sections, and Thin Sections from the Xiahulin Lead-Zinc Mine. **(A)** Reflected light (−), metasomatic dissolution texture; **(B)** Reflected light (−), the second-stage chalcopyrite and sphalerite exhibiting an emulsion-like solid solution unmixing texture; **(C)** Re-flected light (−), anhedral granular texture; **(D)** Fluoritization of the lead-zinc orebody observed underground; **(E)** Transmitted light (−), chloritization of syenogranite; **(F)** Transmitted light (+), sericitization of syenogranite. Py - Pyrite; Ccp - Chalcopyrite; Gn - Galena; Sp - Sphalerite; Mag - Magnetite; Pl - Plagioclase; Qtz - Quartz; Chl - Chlorite; Str - Sericite; Fl - Fluorite.

melting machine that has been heated to 1,100°C, pre melt for 2 min, shake and spin for 8 min, and let it stand for 1 min. After the melting of the sample is completed, use crucible tongs to remove the platinum crucible and place it on the refractory brick. Let it cool naturally for about 5 min, peel it off, label it, and store it in a dryer for testing. For detailed experimental procedures, reference materials, and calculated LOD, please refer to relevant literature (Lv et al., 2023).

The trace element and REEs were analyzed using the XSERISEII ICP-MS instrument manufactured by Thermo Fisher Scientific.

Weigh 0.1 g of the sample into a PTFE inner tank of a closed dissolution apparatus, add 1 mL of HF and 0.5 mL of HNO_3, cover with a PTFE lid, and put it into a stainless steel sleeve. Tighten the steel sleeve lid and keep it at 190°C for 48 h in an oven. Remove, cool down, open the lid, take out the inner can, and heat it on an electric heating plate at 200°C to evaporate. Add 1 mL of HNO_3 and evaporate until dry to drive away hydrofluoric acid. Repeat this step twice, add 5 mL of HCl (1 + 1), seal again in a steel jacket, keep at 130°C for 3 h in an oven, remove and cool, dilute
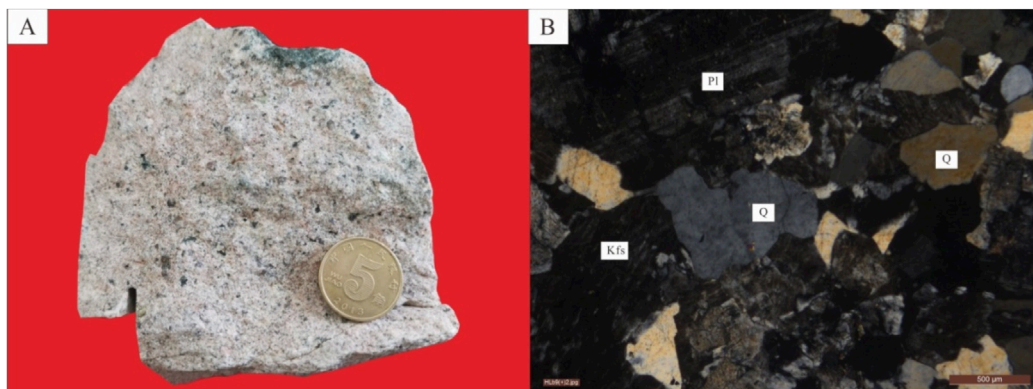
FIGURE 4
Hand Specimen and Microscopic Characteristics of Syenogranite from the Xiahulin Lead-Zinc Mine. **(A)** Photograph of a hand specimen of syenogranite; **(A)** Micrograph of syenogranite under transmitted light (+), showing quartz (Q), potassium feldspar (Kfs), and plagioclase (Pl).

TABLE 1 Major element analysis results (%) of syenogranites from the Xiahulin mining area.

Sample	HLDH257	HLDH258	HLDH259	HLDH260	HLDH261	HLDH262	HLDH263	HLDH264
Syenogranite (HLDH257-264)								
SiO_2	77.22	59.42	77.60	77.59	77.60	78.21	77.62	72.81
TiO_2	0.08	0.05	0.08	0.08	0.08	0.07	0.07	0.07
Al_2O_3	12.49	9.56	12.43	12.51	12.63	12.53	12.47	11.93
Fe_2O_3	0.55	0.23	0.68	0.82	0.60	0.56	0.64	0.88
MnO	0.03	0.01	0.01	0.02	0.02	0.02	0.02	0.02
MgO	<0.08	<0.08	<0.08	<0.08	<0.08	<0.08	<0.08	<0.08
CaO	0.37	0.23	0.23	0.26	0.23	0.23	0.23	0.24
Na_2O	3.21	2.37	4.01	3.99	3.60	3.19	3.21	3.59
K_2O	4.79	3.74	4.52	4.51	4.71	4.85	4.72	4.41
P_2O_5	<0.01	<0.01	<0.01	<0.01	<0.01	<0.01	<0.01	<0.01
LOI	1.20	24.81	0.62	0.27	0.56	0.41	1.07	6.18
Total	99.95	100.42	100.18	100.05	100.03	100.06	100.04	100.14
$Na_2O + K_2O$	8.00	6.11	8.53	8.50	8.31	8.04	7.92	8.01
Na_2O/K_2O	0.67	0.63	0.89	0.89	0.76	0.66	0.68	0.81
Mg#	0.31	0.30	0.33	0.28	0.32	0.34	0.31	0.26
A/NK	1.19	1.20	1.08	1.09	1.15	1.19	1.20	1.12
A/CNK	1.12	1.15	1.05	1.05	1.11	1.15	1.16	1.08
R1	2890	2934	2672	2670	2773	2925	2930	2673
R2	291	284	272	276	277	274	275	279

Note: A/CNK, $Al_2O_3/(CaO + Na_2O + K_2O)$ (mol), A/NK, $Al_2O_3/(Na_2O + K_2O)$ (mol), $R_1 = 4Si-11(Na + K)-2(Fe + Ti)$, $R_2 = 6Ca+2 Mg + Al$.

FIGURE 5
Presents various diagrams for the syenogranites from the Xiahulin lead-zinc deposit, including the TAS diagram **(A)** (based on Wilson, 1989), K$_2$O-SiO$_2$ diagram **(B)** (based on Peccerillo and Taylor, 1976), K$_2$O-Na$_2$O diagram **(C)** (based on Middlemost, 1972), and A/NK-A/CNK diagram **(D)** (based on Maniar and Piccoli, 1989).
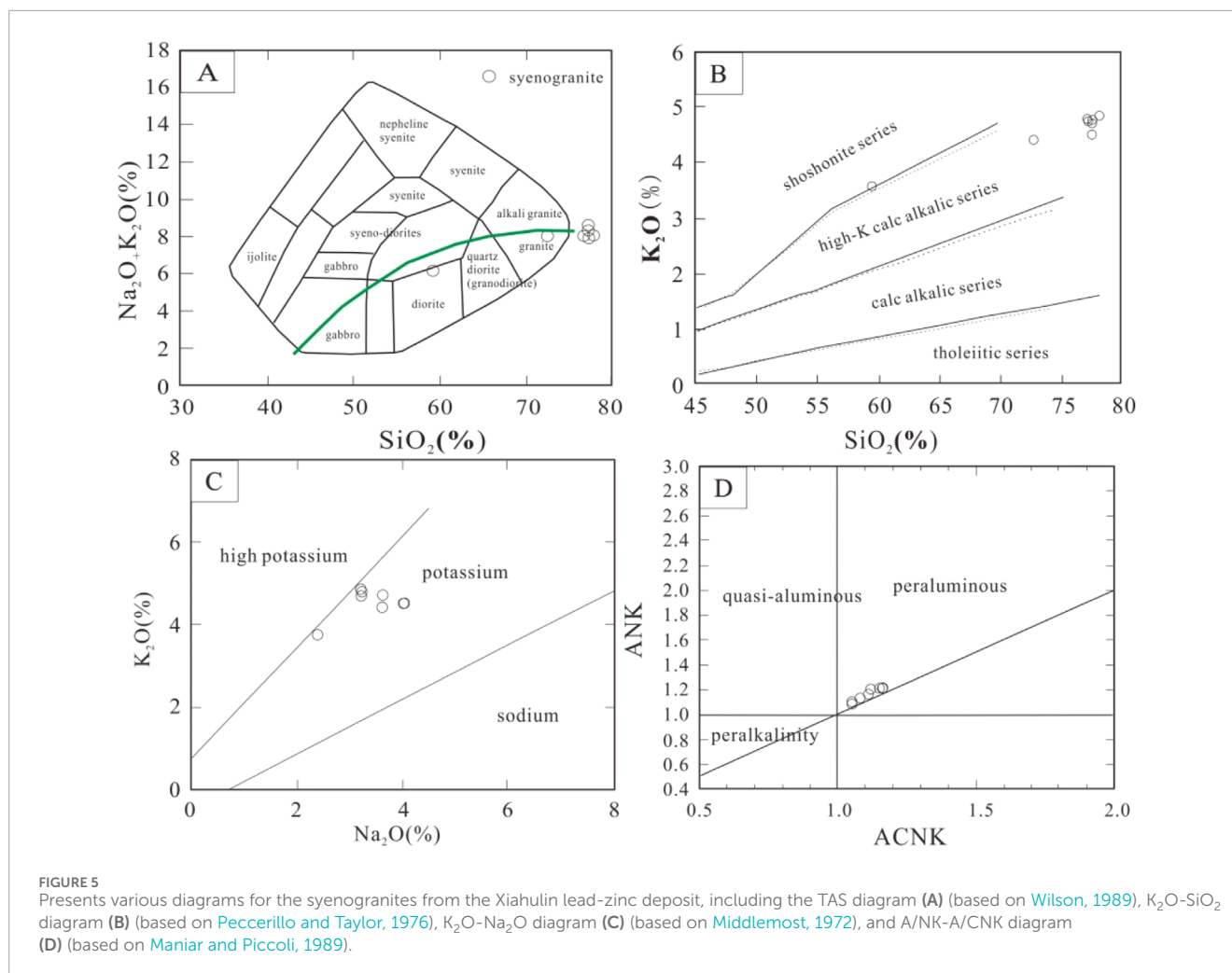
to 25 mL, and prepare 2 blank samples along with the experiment. For detailed experimental procedures, reference materials, and LOD, please refer to relevant literature (Zhao et al., 2021). The solution to be measured is introduced into the high-temperature plasma, and the mass spectrometer automatically calculates the concentration of each element. The analysis error of trace elements is generally less than 5%.

4.2 *In-situ* S and Pb isotope analysis

To determine the source of metallogenic materials in the Xiahulin lead-zinc deposit, *in-situ* micro-scale sulfur (S) and lead (Pb) isotope analyses were performed on metal sulfides from the main mineralization stage. Sulfur isotope analysis was conducted using LA-MC-ICP-MS at Kehui Testing Technology (Tianjin) Co., Ltd., employing a Neptune Plus multi-collector ICP-MS (Thermo Scientific) paired with a RESOlution SE 193 nm laser (testing environment: temperature requirement of 18°C–22°C, relative humidity<65%). Select a suitable area based on the scanned photos of the sample, and use a laser ablation system to ablate sulfides. Point erosion is used for erosion, with a diameter of 30 μm (sphalerite)/20 μm (pyrite), energy density of

3 J/cm^2, and frequency of 5 Hz. Using high-purity He as the carrier gas, the aerosol generated by erosion is blown out and sent to MC-ICP-MS for mass spectrometry testing. ^{32}S and ^{34}S are simultaneously received statically using Faraday cups, with an integration time of 0.131 s 200 sets of data are collected, taking approximately 27 s in total. Before formal testing, adjust the instrument parameters with sulfide standard samples to achieve the optimal state. To reduce the impact of matrix effects on test results, sulfides similar to the sample matrix were used as standard samples during the analysis process, and quality discrimination correction was performed using the standard-sample-standard cross method.

In situ lead isotope analyses of sulfide were performed on a Neptune Plus MC-ICP-MS (Thermo Fisher Scientific, Bremen, Germany) equipped with a Geolas HD excimer ArF laser ablation system (Coherent, Göttingen, Germany) at the Wuhan SampleSolution Analytical Technology Co., Ltd., Hubei, China. In the laser ablation system, helium was used as the carrier gas for the ablation cell and was mixed with argon (makeup gas) after the ablation cell. The spot diameter ranged from 44 to 90 μm dependent on Pb signal intensity. The pulse frequency was from 4 to 10 Hz, but the laser fluence was kept constant at ~5 J/cm^2. A new signal-smoothing and mercury-removing device was used downstream

TABLE 2 Rare earth and trace element analysis results (10^{-6}) of syenogranite and sphalerite in the main mineralization stage of Xiahulin mining area.

Sample	HLDH257	HLDH258	HLDH259	HLDH260	HLDH261	HLDH262	HLDH263	HLDH264	21XHL1	21XHL2	21XHL3	21XHL4	21XHL5	22XHL1	23XHL1
	Syenogranite (HLDH257–264), sphalerite (21XHL1-21XHL5, 22XHL1, 23XHL1)														
Rb	274.47	267.10	239.19	234.14	261.25	272.56	260.78	254.27	0.27	0.12	0.13	0.21	1.10	0.15	0.23
Ba	130.80	149.30	137.00	138.80	138.50	133.40	140.80	153.30	3.04	1.79	1.78	1.86	3.60	2.97	2.11
Th	35.25	25.84	30.05	30.50	30.49	31.38	32.79	32.81	0.39	0.22	0.21	0.18	0.15	0.20	0.18
U	2.09	1.90	2.49	2.14	1.75	1.64	2.07	3.95	0.90	0.25	0.20	0.62	0.07	3.59	0.59
Nb	9.49	10.37	28.23	28.87	11.23	11.31	9.27	26.19	0.23	0.10	0.00	0.10	0.00	0.00	0.00
Sr	17.76	12.38	12.18	15.10	12.30	11.76	12.14	17.68	2.99	1.65	0.85	1.32	1.67	2.36	1.59
Zr	119.07	114.84	124.70	132.53	116.69	110.85	118.53	140.22	1.61	0.56	0.81	0.58	0.26	0.56	0.46
Be	4.26	3.73	3.78	3.49	4.40	4.03	3.82	4.81	0.21	0.10	0.09	0.11	0.08	0.12	0.12
Co	1.16	1.20	0.98	3.32	1.77	1.23	1.25	1.64	101.23	85.49	83.41	77.25	91.16	63.01	77.10
Cu	1.89	2.26	1.98	2.83	2.87	2.06	2.41	3.41	1195.74	57.79	88.36	108.08	96.39	541.51	108.68
Ga	21.16	20.07	21.10	20.39	20.56	20.48	20.75	20.09	2.17	0.58	0.56	0.48	0.51	1.18	0.49
Li	7.47	6.77	3.54	4.15	4.44	6.67	6.99	4.62	1.16	0.65	0.62	0.80	0.61	0.60	0.82
Mo	0.35	0.28	0.41	0.43	0.48	0.29	0.34	0.50	0.91	7.74	1.26	2.08	2.55	11.46	2.13
Ni	1.01	1.41	0.98	1.03	1.51	0.96	1.03	1.51	1.92	1.06	2.07	1.94	1.91	2.04	1.96
Pb	45.51	39.56	35.58	36.52	37.83	38.69	44.12	26.79	26413.90	21753.80	19923.25	64673.94	16019.22	13939.21	49664.83
Sc	10.68	9.35	8.65	8.67	10.26	11.97	11.30	7.97	1.05	0.55	0.46	0.46	0.44	0.49	0.50
Sn	5.15	4.90	3.89	3.94	5.53	4.82	4.74	5.56	4.79	0.98	1.85	2.06	1.52	6.54	2.05
Ta	1.72	1.62	1.65	1.93	2.20	1.52	2.09	2.29	-	—	—	—	—	—	—
V	2.89	3.90	4.39	1.72	3.96	2.76	1.97	6.08	1.46	0.47	0.20	0.34	0.26	0.34	0.50
W	8.78	8.86	7.94	31.69	15.73	9.85	9.79	12.58	0.34	0.28	0.08	0.19	0.24	0.05	0.13
Zn	38.60	32.10	18.61	26.02	24.12	28.97	33.38	18.58	597271.32	628378.17	620888.46	574223.72	622407.06	607826.50	588692.32
La	24.31	16.70	25.40	23.52	22.30	15.90	18.08	21.09	4.58	1.90	0.94	0.55	0.17	0.88	0.33

(Continued on the following page)

TABLE 2 *(Continued)* Rare earth and trace element analysis results (10^{-6}) of syenogranite and sphalerite in the main mineralization stage of Xiahulin mining area.

Sample	HLDH257	HLDH258	HLDH259	HLDH260	HLDH261	HLDH262	HLDH263	HLDH264	21XHL1	21XHL2	21XHL3	21XHL4	21XHL5	22XHL1	23XHL1
	Syenogranite (HLDH257–264), sphalerite (21XHL1–21XHL5, 22XHL1, 23XHL1)														
Ce	53.14	50.13	55.52	51.46	52.04	45.97	56.29	53.81	9.96	3.19	1.67	1.49	0.39	1.79	0.91
Pr	7.44	5.05	6.84	6.46	6.13	4.70	5.48	5.72	1.17	0.42	0.21	0.17	0.04	0.20	0.11
Nd	26.52	19.44	27.22	25.90	24.09	17.71	21.24	21.92	4.74	1.59	0.86	0.69	0.22	0.81	0.49
Sm	6.63	4.97	6.87	6.60	6.16	4.34	5.56	5.74	1.29	0.34	0.21	0.16	0.05	0.19	0.12
Eu	0.15	0.13	0.14	0.14	0.14	0.12	0.14	0.15	0.24	0.06	0.04	0.03	0.01	0.04	0.03
Gd	5.70	4.83	6.09	5.76	5.31	4.13	5.37	5.21	1.31	0.31	0.18	0.14	0.04	0.18	0.13
Tb	1.15	1.15	1.25	1.22	1.11	0.94	1.26	1.20	0.22	0.05	0.03	0.03	0.01	0.04	0.03
Dy	7.70	8.48	8.49	8.34	7.62	6.76	9.08	8.88	1.17	0.25	0.19	0.16	0.03	0.21	0.17
Ho	1.54	1.73	1.76	1.74	1.54	1.39	1.82	1.88	0.18	0.04	0.03	0.03	0.01	0.04	0.04
Er	4.68	5.35	5.56	5.50	4.75	4.34	5.54	6.08	0.40	0.10	0.09	0.09	0.02	0.13	0.10
Tm	0.78	0.90	0.96	0.95	0.82	0.71	0.92	1.07	0.04	0.01	0.01	0.01	0.00	0.02	0.01
Yb	5.28	6.01	6.50	6.19	5.57	4.82	5.94	7.13	0.21	0.07	0.06	0.07	0.01	0.12	0.08
Lu	0.77	0.90	0.95	0.93	0.84	0.71	0.87	1.04	0.02	0.01	0.01	0.01	0.00	0.01	0.01
Y	41.36	48.91	47.73	46.36	43.13	37.74	50.47	49.88	5.21	1.29	1.03	0.98	0.27	1.37	1.18
ΣREE	145.78	125.75	153.54	144.71	138.42	112.52	137.60	140.92	25.55	8.35	4.54	3.63	1.01	4.65	2.56
LREE	118.18	96.42	121.99	114.09	110.86	88.73	106.80	108.43	21.98	7.51	3.94	3.10	0.88	3.90	1.99
HREE	27.59	29.33	31.55	30.62	27.56	23.78	30.80	32.49	3.57	0.84	0.60	0.53	0.12	0.75	0.57
LREE/HREE	4.28	3.29	3.87	3.73	4.02	3.73	3.47	3.34	6.16	8.93	6.51	5.79	7.29	5.20	3.48
La_N/Yb_N	3.30	1.99	2.80	2.73	2.87	2.37	2.18	2.12	15.43	20.90	10.99	5.53	9.46	5.36	2.84
δEu	0.08	0.08	0.07	0.07	0.08	0.08	0.08	0.09	0.56	0.59	0.59	0.57	0.93	0.59	0.66
δCe	0.97	1.34	1.03	1.02	1.09	1.30	1.39	1.20	1.06	0.87	0.91	1.19	1.18	1.05	1.18
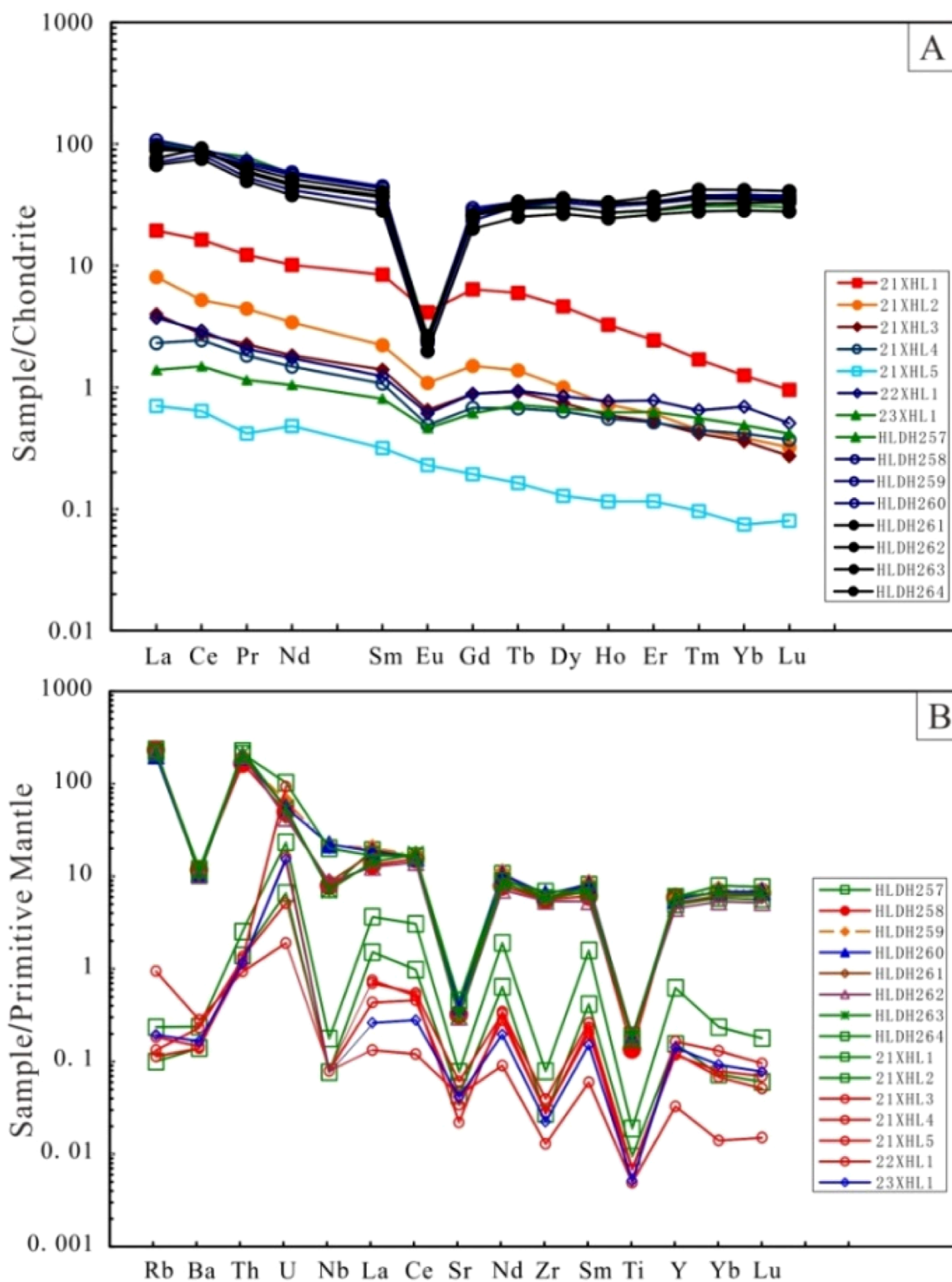
FIGURE 6
Displays the chondrite-normalized rare earth element (REE) patterns [**(A)**, the value of chondrite meteorites from Boynton, 1984] and primitive mantle-normalized trace element spider diagrams [**(B)**, prim-itive mantle data from Sun and McDonough, 1989] for the syenogranites and sphalerite from the main mineralization stage of the Xiahulin mining area.

TABLE 3 S isotope test results from the third metallogenic stage of the Xiahulin lead-zinc deposit.

Deposit	Sample	$\delta^{34}S_{V\text{-}CDT}$ (‰)	Source
Qiyimuchang Pb-Zn	sphalerite	4.8	Duan et al. (2022)
	pyrite	4.3	
	sphalerite	4.7	
	sphalerite	4.4	
	pyrite	4.3	
	sphalerite	3.8	
	pyrite	1.6	
Jiawula Pb-Zn	galena	3.9	Zhai et al. (2013)
	galena	4.1	
	pyrite	3.7	
	pyrite	3.2	
	pyrite	2.8	
	sphalerite	3.9	
	sphalerite	3.8	
Dongjun Pb-Zn	galena	4.5	Zhang (2011)
	pyrite	6.8	
	pyrite	6.6	
	pyrite	7.0	
	pyrite	6.9	
Derbur Pb-Zn	pyrite	5.2	Zhang et al. (2002)
	pyrite	5.4	
	pyrite	4.9	
	pyrite	5.2	
	sphalerite	5.0	
	sphalerite	5.2	
	galena	2.9	
	galena	3.6	
Xiahulin Pb-Zn	pyrite	3.5	This paper
	pyrite	5.5	
	pyrite	3.5	
	sphalerite	5.0	
	sphalerite	6.0	

TABLE 3 (*Continued*) S isotope test results from the third metallogenic stage of the Xiahulin lead-zinc deposit.

Deposit	Sample	$\delta^{34}S_{V\text{-}CDT}$ (‰)	Source
	sphalerite	5.7	
	pyrite	5.4	
	sphalerite	5.8	
Badaguan Cu-Mo	pyrite	2.0	Hou (2014)
	pyrite	1.9	
	pyrite	1.5	
	pyrite	1.7	
	pyrite	1.9	

from the sample cell to efficiently eliminate the short-term variation of the signal and remove the mercury from the background and sample aerosol particles. The Neptune Plus was equipped with nine Faraday cups fitted with $10^{11}\,\Omega$ resistors. Isotopes ^{208}Pb, ^{207}Pb, ^{206}Pb, ^{204}Pb, ^{205}Tl, ^{203}Tl, and ^{202}Hg were collected in Faraday cups using static mode. The mass discrimination actor for Pb was determined using a Tl solution nebulized at the same time as the sample, using an Aridus II desolvating nebulizer. The mass fractionation of Pb isotopes was corrected by ^{205}Tl/^{203}Tl with the exponential law. Note that the optimized values of ^{205}Tl/^{203}Tl, which were calibrated from measuring two Pb isotope standards MASS-1 (USGS) and Sph-HYLM (sphalerite, in-house standard), replaced the natural Tl isotopic composition for the mass fractionation correction of Pb isotopes. The ^{202}Hg signal was used to correct the remaining ^{204}Hg interference on ^{204}Pb, using the natural ^{202}Hg/^{204}Hg ratio (0.2301). In addition, the mass fractionation of ^{204}Hg/^{202}Hg was corrected by the ^{205}Tl/^{203}Tl normalization. In this case, we assumed identical mass fractionation factors for ^{204}Hg/^{202}Hg and ^{205}Tl/^{203}Tl. Sph-HYLM was used to monitor the precision and accuracy of the measurements after ten sample analyses, over the entire period of analysis. The obtained accuracy is estimated to be equal to or better than ±0.2‰ for ^{208}Pb/^{204}Pb, ^{207}Pb/^{204}Pb, and ^{206}Pb/^{204}Pb compared to the solution value by MC-ICP-MS, with a typical precision of 0.4‰ (2σ). The more detail of the *in situ* Pb isotopic ratios analysis was described in Zhang et al. (2016). All data reduction for the MC-ICP-MS analysis of Pb isotope ratios was conducted using "Iso-Compass" software (Zhang et al., 2020).

4.3 Zircon U-Pb dating and Hf isotope analysis
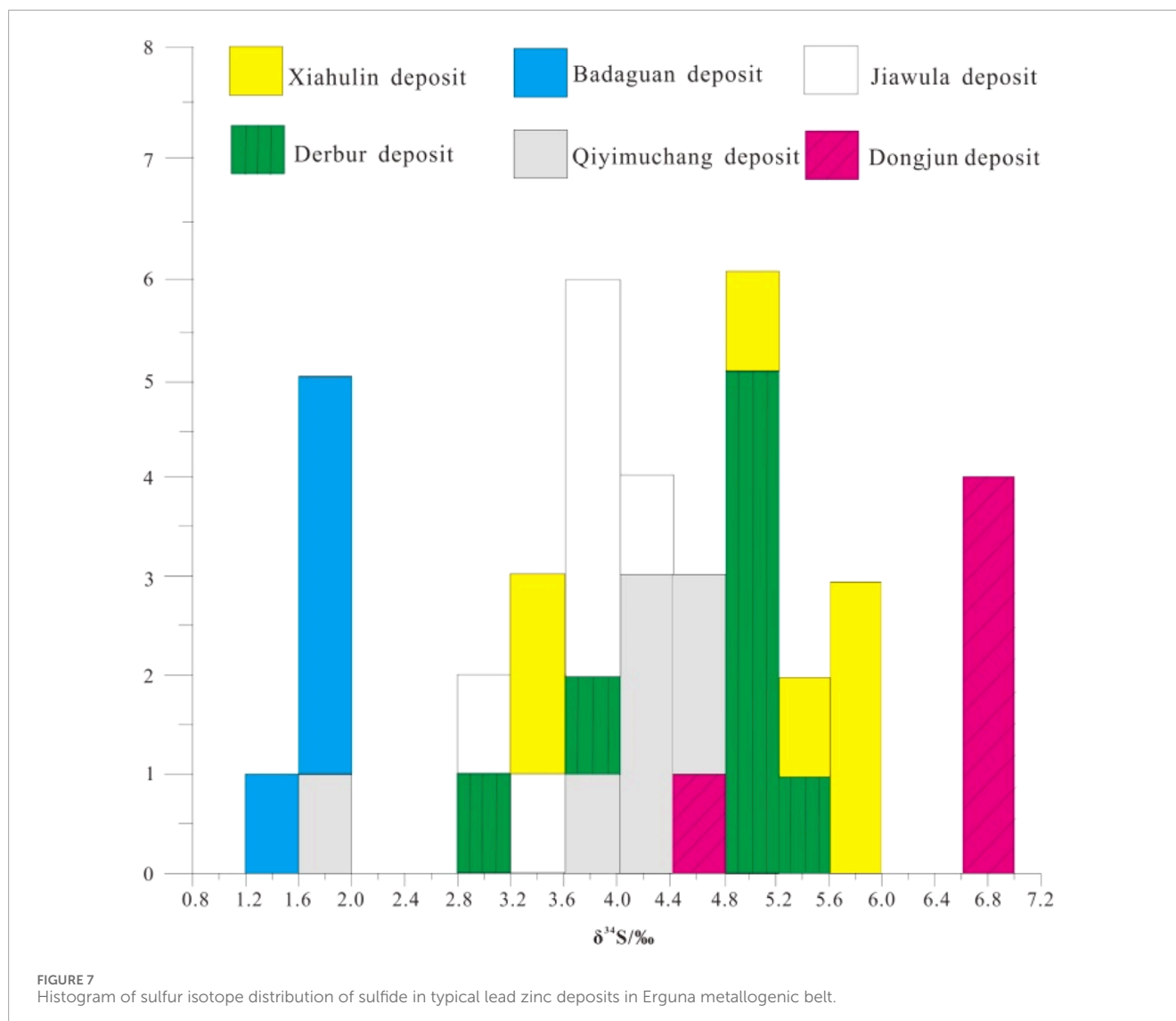
To establish the petrogenesis and timing of mineralization in the Xiahulin lead-zinc deposit, zircon U-Pb dating was performed on the mineralization-associated rocks collected from the 90-meter adit of the No. 3 inclined shaft. The syenogranite exhibited a fresh, light-reddish color (Figure 4A) with a medium-grained granite texture and massive structure. It was primarily composed of quartz

TABLE 4 Pb isotope test results from the third metallogenic stage of the Xiahulin lead-zinc deposit.

Deposit	Sample	Mineral	$^{206}Pb/^{204}Pb$	$^{207}Pb/^{204}Pb$	$^{208}Pb/^{204}Pb$	μ	ω	Δα	Δβ	Δγ	Data sources
Xiahulin Pb-Zn	21XHL10-Pb1	galena	18.480	15.588	38.378	9.43	35.80	79.71	17.41	32.63	This paper
	21XHL10-Pb2		18.472	15.583	38.363	9.42	35.73	79.23	17.03	32.22	
	21XHL10-Pb3		18.473	15.583	38.362	9.42	35.72	79.32	17.04	32.21	
	21XHL9-Pb1		18.481	15.591	38.386	9.44	35.85	79.78	17.57	32.85	
Badaguan Cu-Mo	M561-4-1	pyrite	18.296	15.524	38.036	9.40	35.13	69.52	13.23	23.73	Hou (2014)
	M561-4-2		18.311	15.525	38.037	9.42	35.14	70.4	13.30	23.76	
	M561-6-1		18.294	15.532	38.045	9.4	35.17	69.4	13.76	23.98	
	M561-6-2		18.281	15.518	37.992	9.38	34.95	68.64	12.84	22.55	
	M561-6-3		18.299	15.530	38.034	9.40	35.12	69.7	13.63	23.68	
		upper crust							>18	>45	Li and Zhao (2014)
		crust-mantle mixed							12–40	20–45	
		mantle							−5–15	−5–20	

Note: The isotope parameters were calculated using the Geokit software developed by Lu Yuanfa (Lu, 2004).

FIGURE 7
Histogram of sulfur isotope distribution of sulfide in typical lead zinc deposits in Erguna metallogenic belt.

(40%, anhedral granular, colorless to smoky gray, 0.5–1.5 mm), plagioclase (20%, grayish white, subhedral tabular, 0.5–2 mm), and potassium feldspar (35%, light reddish, subhedral tabular, 0.5–1.5 mm) (Figure 4B), with minor biotite (5%, anhedral, often in aggregates).

U-Pb dating analyses were conducted by LA-ICP-MS at at Beijing Createch Testing Technology Co.,Ltd. Detailed operating conditions for the laser ablation system and the ICP-MS instrument and data reduction are the same as description by Hou et al. (2009). Laser sampling was performed using a RESOlution 193 nm laser ablation system. An AnalytikJena PQMS Elite ICP-MS instrument was used to acquire ion-signal intensities. Helium was applied as a carrier gas. Argon was used as the make-up gas and mixed with the carrier gas via a T-connector before entering the ICP. Each analysis incorporated a background acquisition of approximately 15–20 s (gas blank) followed by 45 s data acquisition from the sample. Off-line raw data selection and integration of background and analyte signals, and time-drift correction and quantitative calibration for U-Pb dating was performed by ICPMSDataCal (Liu et al., 2010).

Zircon GJ-1 was used as external standard for U-Pb dating, and was analyzed twice every 5–10 analyses. Time-dependent drifts of U-Th-Pb isotopic ratios were corrected using a linear interpolation (with time) for every 5–10 analyses according to the variations of GJ-1 (i.e., 2 zircon GJ-1 + 5–10 samples +2 zircon GJ-1) (Liu et al., 2010). Uncertainty of preferred values for the external standard GJ-1 was propagated to the ultimate results of the samples. In all analyzed zircon grains the common Pb correction was not necessary due to the low signal of common ^{204}Pb and high ^{206}Pb/^{204}Pb. U, Th and Pb concentration was calibrated by NIST 610. Concordia diagrams and weighted mean calculations were made using Isoplot/Ex_ver3. The zircon Plesovice is dated as unkown samples and yielded weighted mean ^{206}Pb/^{238}U age of 337.4 ± 3.4 Ma (2SD, n = 7), which is in good agreement with the recommended ^{206}Pb/^{238}U age of 337.13 ± 0.37 Ma (2SD) (Sláma et al., 2008).

The measurement of Hf isotopes in zircon micro-areas was conducted at the labor-atory of Kehui Testing Technology (Tianjin) Co., Ltd. The detection equipment used in this study is a laser ablation multi-receiver inductively coupled plasma

FIGURE 8
Cathodoluminescence (CL) image of zircons from the syenogranite in the Xiahulin lead-zinc mining area.

mass spectrometer. The laser injection system employed is the RESOlution SE solid-state laser, while the analysis system utilized is the NEPTUNE plus multi-receiver plasma mass spectrometer. Cathodoluminescence (CL) imaging was used to acquire the internal structural information of zircon, and specific analysis locations were chosen accordingly. The duration of laser ablation is 27 s, the diameter of the spot beam is around 30 μm, the energy density is 6 J/cm^2, and the frequency is 6 Hz. To guarantee the correctness of the analysis procedure in this investigation, the researchers employed the Plesovice zircon standard sample as a reference. The detected $^{176}Hf/^{177}Hf$ ratio remained stable within the range of 0.282488 ± 20 (2SD, n = 6). The test results are consistent with the data published by Sláma et al. (2008), within the margin of error.

5 Analysis results

5.1 Characteristics of major, trace, and rare earth elements

Table 1 presents the major element compositions of the Early Jurassic syenogranites from the Xiahulin lead-zinc deposit. The SiO$_2$ contents ranged from 59.42 to 78.21 wt% (most samples exceed 72.81 wt%, with only one at 59.42 wt% likely due to higher loss on ignition), Al$_2$O$_3$ = 9.56 to 12.63 wt%, Fe$_2$O$_3$ = 0.23 to 0.88 wt%, CaO = 0.23 to 0.37 wt%, Na$_2$O = 2.37 to 4.01 wt%, K$_2$O = 3.74 to 4.85 wt%, Na$_2$O + K$_2$O = 6.11 to 8.53 wt%, and Mg$^\#$ = 0.26 to 0.34. In the TAS (Figure 5A) and SiO$_2$-K$_2$O (Figure 5B) diagrams, the samples fell within the high-K calc-alkaline series, whereas in the Na$_2$O-K$_2$O diagram (Figure 5C), they were plotted within the potassic series. The A/CNK values ranged from 1.05 to 1.16,
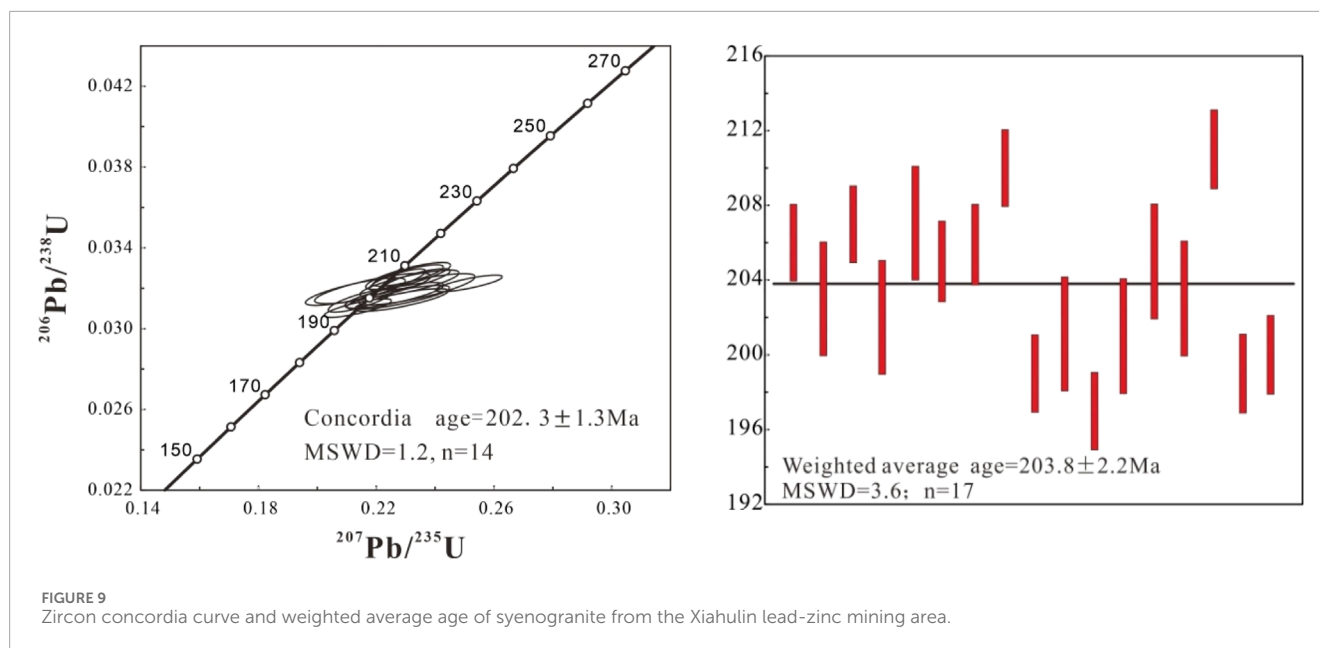
and the A/NK values from 1.08 to 1.20, categorizing them as peraluminous granite (Figure 5D).

Table 2 presents the trace and rare earth element (REE) data for syenogranites associated with mineralization in the Xiahulin lead-zinc deposit, along with individual sphalerite samples. The REE and trace elements in the syenogranite and sphalerite exhibit different characteristics, with syenogranites containing higher REE and trace element concentrations than sphalerite. The total REE content in the syenogranites ranged from 112.52 to 153.54 × 10^{-6}, with an average of 137.40 × 10^{-6}. The syenogranites displayed enrichment of light REEs (LREEs) over heavy REEs (HREEs), with LREEs from 83.73 to 88.73 × 10^{-6}, HREEs from 23.78 to 32.49 × 10^{-6}, and LREE/HREE ratios between 3.29 and 4.28. The chondrite-normalized REE patterns (Figure 6A) exhibited a slight rightward trend, enriched in LREEs and depleted in HREEs, accompanied by a distinct negative Eu anomaly (δEu = 0.07 to 0.09, average 0.08). The total REE content in the sphalerite ranged from 1.01 to 25.55 × 10^{-6}, with an average of 7.18 × 10^{-6}. The sphalerite displayed enrichment of light REEs (LREEs) over heavy REEs (HREEs), with LREEs from 0.88 to 21.98 × 10^{-6}, HREEs from 0.12 to 3.57 × 10^{-6}, and LREE/HREE ratios between 3.48 and 8.93. The chondrite-normalized REE patterns (Figure 6A) exhibited a distinct rightward trend, enriched in LREEs and depleted in HREEs, accompanied by a slight negative Eu anomaly (δEu = 0.57 to 0.93, average 0.64).

In the primitive mantle-normalized trace element spider diagrams (Figure 6B), both syenogranite and sphalerite samples exhibit significant negative Sr anomalies, which may be due to residual source areas such as plagioclase in the rocks and strong rock alteration. The higher Th/U values (8.3–19.11) in syenogranite may indicate its mantle derived origin. The Th/U value (0.05–1.99) in sphalerite is significantly lower than that in syenogranite, and

TABLE 5 LA-ICP-MS zircon U–Pb isotope analysis data of syenogranite from the Xiahulin mining area.

Numbers	U (10⁻⁶)	Th (10⁻⁶)	Th/U	Isotope ratio						Age (Ma)					
				$^{207}Pb/^{206}Pb$	1σ	$^{207}Pb/^{235}U$	1σ	$^{206}Pb/^{238}U$	1σ	$^{206}Pb/^{238}U$	1σ	$^{207}Pb/^{235}U$	1σ	$^{207}Pb/^{206}Pb$	1σ
1	1312.11	788.91	0.60	0.0508	0.0014	0.2272	0.0063	0.0324	0.0004	206	2	208	5	232	44
2	320.54	138.55	0.43	0.0515	0.0033	0.2189	0.0131	0.0320	0.0005	203	3	201	11	261	108
3	1088.27	561.285	0.52	0.0510	0.0016	0.2301	0.0079	0.0326	0.0004	207	2	211	7	240	59
4	460.48	197.055	0.43	0.0490	0.0026	0.2130	0.0112	0.0318	0.0005	202	3	196	9	147	94
5	746.19	477.945	0.64	0.0517	0.0022	0.2309	0.0095	0.0326	0.0004	207	3	211	8	274	70
6	1613.93	1511.87	0.94	0.0563	0.0016	0.2515	0.0075	0.0322	0.0003	205	2	228	6	463	51
7	1424.62	1026.86	0.72	0.0527	0.0018	0.2339	0.0075	0.0325	0.0003	206	2	213	6	315	54
8	1268.79	1317.25	1.04	0.0596	0.0021	0.2716	0.0092	0.0330	0.0004	210	2	244	7	589	53
9	505.07	214.53	0.42	0.0531	0.0025	0.2285	0.0106	0.0314	0.0004	199	2	209	9	336	84
10	465.34	192.29	0.41	0.0518	0.0026	0.2262	0.0111	0.0317	0.0004	201	3	207	9	277	89
11	1062.48	929.06	0.87	0.0500	0.0018	0.2138	0.0076	0.0310	0.0003	197	2	207	6	193	64
12	640.70	327.79	0.51	0.0453	0.0024	0.1965	0.0107	0.0317	0.0004	201	3	182	9	−3	90
13	473.55	290.27	0.61	0.0528	0.0026	0.2313	0.0111	0.0322	0.0004	205	3	211	9	323	85
14	312.90	193.50	0.62	0.0535	0.0030	0.2338	0.0131	0.0320	0.0005	203	3	213	11	350	98
15	2540.93	1849.39	0.73	0.0646	0.0019	0.2973	0.0089	0.0332	0.0003	211	2	264	7	762	49
16	1112.88	975.01	0.88	0.0496	0.0017	0.2146	0.0073	0.0314	0.0004	199	2	197	6	179	57
17	602.74	401.97	0.67	0.0524	0.0027	0.2275	0.0115	0.0316	0.0004	200	2	208	10	303	93

FIGURE 9
Zircon concordia curve and weighted average age of syenogranite from the Xiahulin lead-zinc mining area.

the Zr content in sphalerite is also significantly lower than that in syenogranite, which should be due to the replacement and precipitation of minerals such as zircon during silicification and mineralization processes. The depletion of Ti and Nb elements in both syenogranite and sphalerite may indicate the involvement of crustal materials in magmatic processes.

5.2 Characteristics of S and Pb isotopes

In this study, pyrite and sphalerite from the third metallogenic stage of the Xiahulin lead-zinc deposit were selected for *in-situ* S and Pb isotope analysis using laser ablation-multi-collector inductively coupled plasma mass spectrometry (LA-MC-ICP-MS), and the results are presented in Tables 3, 4. As indicated in Table 3, the sulfur isotope composition of metal sulfides in the main mineralization stage of the Xiahulin lead-zinc deposit is similar to that of typical hydrothermal vein type lead-zinc deposits in the region (Figure 7). The δ^{34}S values of metal sulfides in the Xiahulin lead-zinc deposit are all greater than 0, ranging from +3.5‰ to +6.0‰, with an average value of +5.0‰, a range of R = 2.50, and a standard deviation of S = 0.95. It has a small fluctuation range, but has exceeded the fluctuation range of deep source sulfur. The ore-forming material may have been added by crustal materials or sedimentary rocks such as strata. The ^{208}Pb/^{204}Pb, ^{207}Pb/^{204}Pb, and ^{206}Pb/^{204}Pb ratios remained stable at 38.362–38.386, 15.583–15.591, and 18.472–18.481, respectively. These minor variations within a concentrated range indicated that sulfides in the Xiahulin lead-zinc deposit exhibited normal lead characteristics (Du, 1988; Tan, 2011).

5.3 Zircon U-Pb age

The zircons from the syenogranite in the Xiahulin mining area were highly transparent and well crystallized, appearing in aggregated and octahedral forms. The particle sizes ranged from 102

to 205 μm, indicating strong self-formation and distinct oscillatory zoning (Figure 8). The Th content of the zircons varied from 138.55 to 1849.39 ppm, while the U content ranged from 312.9 to 2540.93 ppm. The Th/U ratios, all above 0.4 and spanning from 0.41 to 1.04 (Table 5), indicated a magmatic origin (Wu and Zheng, 2004; Li, 2009).

The surface ages of the 17 measurement points were determined by the ^{206}Pb/^{238}U method, ranging from 197 to 211 Ma, with most clustering between 199 and 207 Ma. On the zircon U-Pb age concordia diagram, all data points were on or near the concordia line (Figure 9). The weighted average age was (203.8 ± 2.2) Ma (MSWD = 3.6; n = 17), indicating the crystallization age of the syenogranite closely associated with the mineralization of the Xiahulin lead-zinc deposit during the Early Jurassic.

5.4 Zircon Hf isotope characteristics

The *in-situ* Hf isotope data for zircons from syenogranite (D0901) were collected from the inclined shaft of the Xiahulin lead-zinc mine and closely associated with mineralization, as detailed in Table 6. The magmatic zircons in sample D0901 exhibited the ^{176}Hf/^{177}Hf ratios from 0.282628 to 0.282846, with εHf(t) values ranging from −1.23 to +6.72. The two-stage Hf model ages (TDM2) ranged from 804 to 1309 Ma. The captured zircon (~437 Ma) demonstrated a ^{176}Hf/^{177}Hf ratio of 0.282620, εHf(t) value of +3.54, and a TDM2 of 1192 Ma. These results indicated that the primary magma was largely derived from partial melting of juvenile crustal material, with minor incorporation of ancient crustal components during magma evolution. The Hf isotope composition of this rock aligned with that of ore-related rocks in the Late Triassic to Early Jurassic porphyry copper-molybdenum deposits in the area (Figure 10).

TABLE 6 Zircon Hf isotope analysis results of ore-forming related rock bodies in the Xiahulin lead-zinc deposit and copper-molybdenum deposits within the study area.

Sample	Age (Ma)	$^{176}Yb/^{177}Hf$	$^{176}Lu/^{177}Hf$	$^{176}Hf/^{177}Hf$	2σ	$\varepsilon_{Hf}(0)$	$\varepsilon_{Hf}(t)$	T_{DM1} (Ma)	T_{DM2} (Ma)	$f_{Lu/Hf}$	Data sources
Xiahulin deposit syenogranite (D0901)											
D0901-03	195	0.107423	0.003256	0.282628	0.001463	−5.09	−1.23	940	1309	−0.90	This paper
D0901-05	195	0.052023	0.001449	0.282721	0.000803	−1.81	2.29	762	1086	−0.96	
D0901-06	195	0.103236	0.002933	0.282820	0.000340	1.70	5.61	645	875	−0.91	
D0901-07	195	0.052217	0.001471	0.282846	0.000111	2.62	6.72	583	804	−0.96	
D0901-10	437	0.081911	0.002455	0.282620	0.001052	−5.37	3.54	930	1192	−0.93	
Wunugetushan deposit adamellite (WS05)											
WS05-001	197.97	0.067606	0.002426	0.282738		−1.20	2.80	756	1057	−0.93	Zhang et al. (2022)
WS05-002	197.19	0.060028	0.002184	0.282694		−2.80	1.30	816	1155	−0.93	
WS05-003	201.82	0.073935	0.002745	0.282820		1.70	5.80	643	874	−0.92	
WS05-004	202.61	0.059110	0.002155	0.282728		−1.50	2.60	765	1074	−0.94	
WS05-005	197.62	0.067911	0.002509	0.282731		−1.40	2.60	768	1073	−0.92	
WS05-006	201.01	0.052678	0.002027	0.282712		−2.10	2.00	786	1110	−0.94	
WS05-007	203.37	0.046370	0.001688	0.282703		−2.40	1.80	792	1127	−0.95	
WS05-008	199.5	0.099606	0.003588	0.282743		−1.00	2.90	775	1055	−0.89	
WS05-009	201.56	0.047960	0.001782	0.282714		−2.00	2.10	778	1103	−0.95	
WS05-010	202.88	0.058686	0.002184	0.282702		−2.50	1.70	805	1135	−0.93	
WS05-011	202.01	0.059888	0.002143	0.282712		−2.10	2.00	789	1111	−0.94	
WS05-012	203.3	0.077946	0.002817	0.282659		−4.00	0.10	882	1235	−0.92	
WS05-013	200.15	0.056164	0.002059	0.282711		−2.10	2.00	788	1113	−0.94	
WS05-014	202.72	0.085910	0.003052	0.282701		−2.50	1.50	825	1143	−0.91	
WS05-015	198.65	0.091676	0.003159	0.282751		−0.70	3.20	753	1034	−0.90	

TABLE 6 *(Continued)* Zircon Hf isotope analysis results of ore-forming related rock bodies in the Xiahulin lead–zinc deposit and copper-molybdenum deposits within the study area.

Sample	Age (Ma)	$^{176}Yb/^{177}Hf$	$^{176}Lu/^{177}Hf$	$^{176}Hf/^{177}Hf$	2σ	ε_{Hf} (0)	ε_{Hf} (t)	T_{DM1} (Ma)	T_{DM2} (Ma)	$f_{Lu/Hf}$	Data sources
Taipingchuan deposit granodiorite porphyry (TPC18-24)											
TPC18-24-01	187.64	0.046997	0.001309	0.282641		−4.60	−0.70	874	1275	−0.96	
TPC18-24-02	190.63	0.042690	0.001225	0.282644		−4.50	−0.50	867	1265	−0.96	
TPC18-24-03	191.62	0.038475	0.001120	0.282721		−1.80	−2.20	756	1091	−0.97	
TPC18-24-04	190.57	0.032154	0.000976	0.282675		−3.40	−0.60	817	1193	−0.97	
TPC18-24-05	189.6	0.033469	0.001073	0.282659		−4.00	0.00	843	1232	−0.97	
TPC18-24-06	189.68	0.040655	0.001259	0.282654		−4.20	−0.20	853	1243	−0.96	
TPC18-24-07	190.73	0.034517	0.001113	0.282608		−5.80	−1.70	915	1344	−0.97	
TPC18-24-08	190.98	0.041086	0.001254	0.282662		−3.90	0.10	842	1225	−0.96	
TPC18-24-09	189.49	0.035968	0.001048	0.282640		−4.70	−0.60	868	1272	−0.97	Cao (2020)
TPC18-24-10	190.84	0.053841	0.001518	0.282671		−3.60	0.40	835	1206	−0.95	
TPC18-24-11	189.11	0.032478	0.000929	0.282631		−5.00	−1.00	879	1293	−0.97	
TPC18-24-12	191.21	0.034823	0.001159	0.282654		−4.20	−0.10	851	1241	−0.97	
TPC18-24-13	189.56	0.042731	0.001264	0.282602		−6.00	−2.00	928	1361	−0.96	
TPC18-24-14	190.44	0.042981	0.001197	0.282697		−2.60	1.40	791	1145	−0.96	
TPC18-24-15	191.79	0.046466	0.001262	0.282705		−2.40	1.70	781	1128	−0.96	
TPC18-24-17	189.95	0.040927	0.001085	0.282631		−5.00	−1.00	882	1294	−0.97	
TPC18-24-18	189.8	0.019918	0.000560	0.282663		−3.90	0.20	826	1218	−0.98	
TPC18-24-19	190.12	0.040128	0.001087	0.282669		−3.60	0.40	828	1208	−0.97	

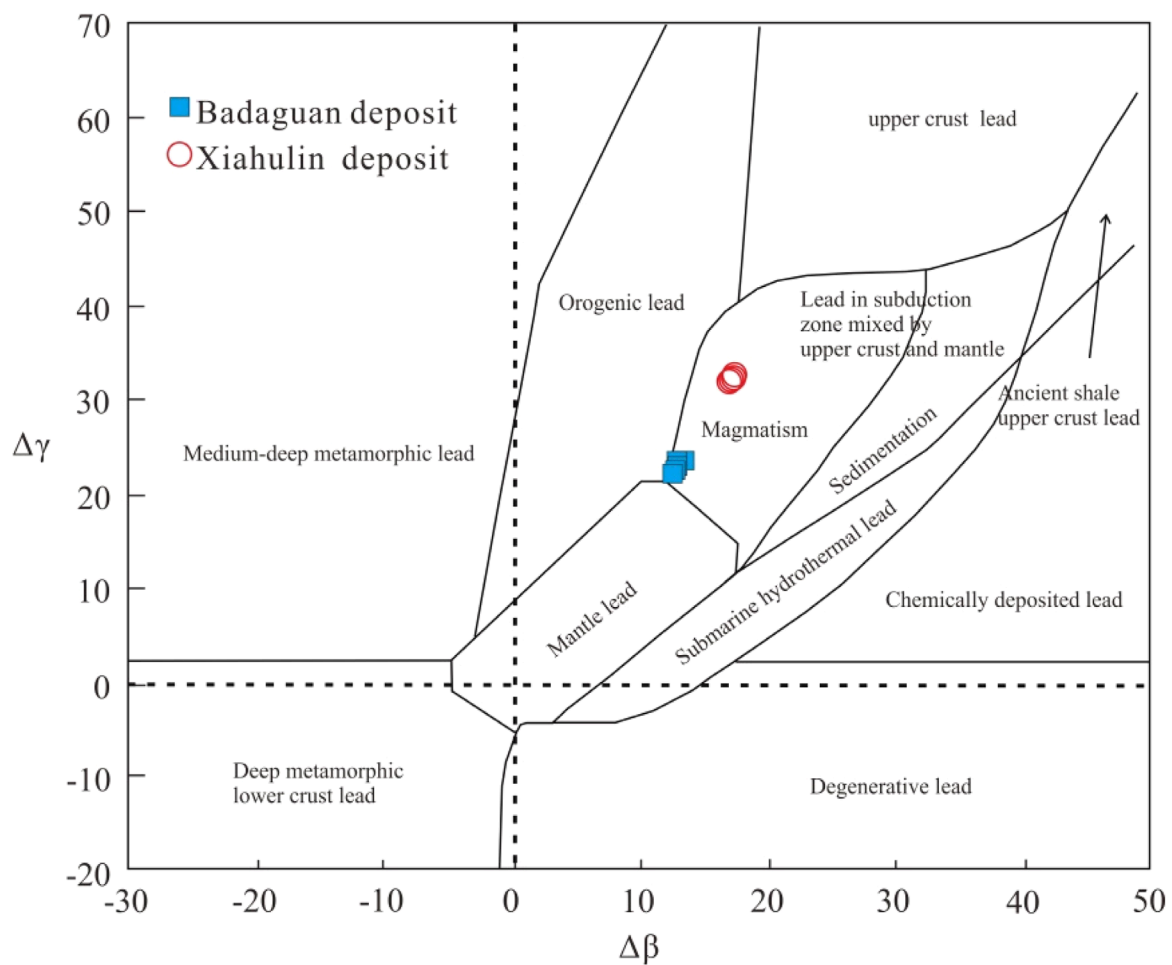**FIGURE 10**
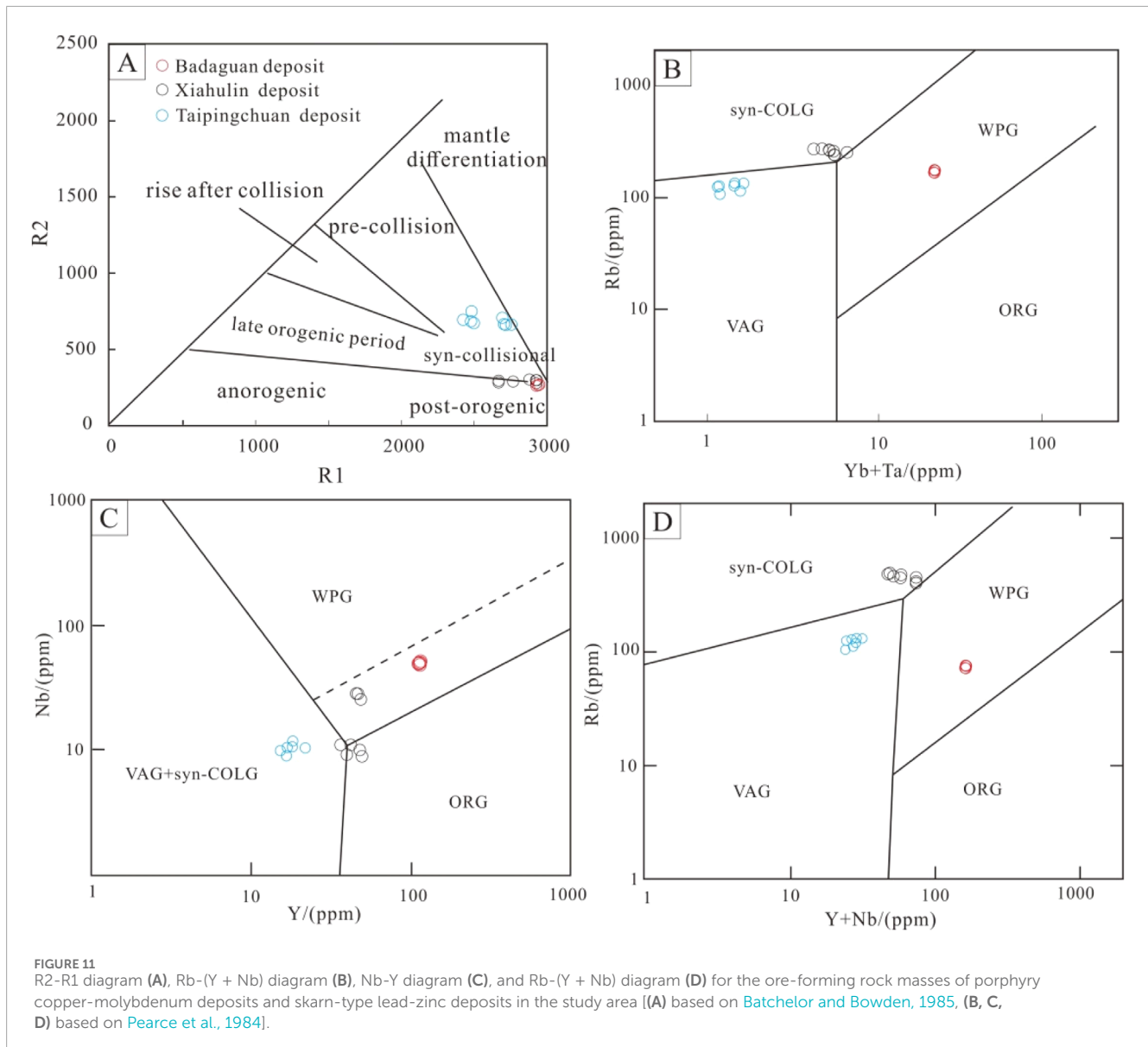Discriminant diagram of lead isotope Δγ-Δβ genesis for Xialin lead-zinc deposit (base map from Zhu et al., 1998).

6 Discussion

6.1 Source of ore-forming materials

Sulfur is a key ore-forming element in lead-zinc deposits, offering insights into sulfur sources and deposit genesis through its isotopic composition (Yang et al., 2018). The stable sulfur isotope composition of metal sulfides reflects the initial isotopic ratios and, along with other indicators, can reveal the provenance of ore-forming materials (Cao et al., 2000; Basuki et al., 2008). Sulfur isotopes generally originate from three main sources: mantle-derived sulfur ($\delta^{34}S \approx 0‰ \pm 3‰$), modern seawater ($\delta^{34}S \approx +20‰$), and reduced sulfur with significantly negative $\delta^{34}S$ values (Chaussidon and Lorand, 1990). The fluctuation range of $\delta^{34}S$ values (+3.5‰~+6.0‰) of sulfur isotopes in sulfide during the main mineralization stage of the Xiahulin lead-zinc deposit is relatively small and close to 0, but it exceeds the fluctuation range of mantle sulfur and has a mixed characteristic of mantle sulfur and crustal sulfur, indicating the presence of crustal or sedimentary rock materials added during the mineralization process. The formation age of the Xiahulin lead-zinc deposit ore-forming rock body is Late

Triassic-Early Jurassic, which should be produced at the same time as the related rock bodies of copper molybdenum deposits in the same period in the region. After comparative research, the $\delta^{34}S$ characteristics of the Xiahulin lead-zinc deposit are slightly different from those of the Badaguan copper molybdenum deposit ($\delta^{34}S$ is 1.5‰–2.0‰) and the Wunugetushan copper molybdenum deposit ($\delta^{34}S$ is −0.2‰~+3.4‰) (Xiang et al., 1998) in the middle section of the Erguna metallogenic belt in the region. The $\delta^{34}S$ value is higher than that of the ore-forming rock bodies of the Wunugetushan and Badaguan deposits. Therefore, it can be said that there are crustal or sedimentary rock materials in the ore-forming process of the Xiahulin lead-zinc deposit. Join, it belongs to a mixed source.

Pb isotopes play a critical role in determining the metallogenic age and sourcing ore-forming materials, especially through the analysis of Pb isotope composition (Doe and Stacey, 1974; Zartman and Doe, 1981). Variations in the Pb isotope characteristic value μ indicate different sources: mantle (μ = 8.92) (Doe, 1979), orogenic belt (μ = 10.87), normal Pb (8.686–9.238) (Isotope Geology Laboratory of Yichang Institute of Geology and Mineral Resources, Ministry of Geology and Mineral Re-sources, 1979), and upper crust (μ = 9.58), each exhibiting distinct ranges.

FIGURE 11
R2-R1 diagram **(A)**, Rb-(Y + Nb) diagram **(B)**, Nb-Y diagram **(C)**, and Rb-(Y + Nb) diagram **(D)** for the ore-forming rock masses of porphyry copper-molybdenum deposits and skarn-type lead-zinc deposits in the study area [(A) based on Batchelor and Bowden, 1985, **(B, C, D)** based on Pearce et al., 1984].

In the Xiahulin deposit, μ values are tightly clustered (9.38–9.42, avg. 9.40), bridging the mantle and upper crust, while ω values (34.95–35.17, avg. 35.10) exceeded the mantle values but remained below the crustal average (Zartman and Doe, 1981), suggesting a mixed Pb origin from both crustal and mantle sources.

To assess the temporal effects and trace the sources of ore-forming materials, the Δβ and Δγ values were computed using Geokit software (Table 4). In the Δγ–Δβ diagram by Zhu et al. (1998), Xiahulin sulfides fell within the mixed crust-mantle source range (Δβ: 17.36–17.88, avg. 17.60; Δγ: 25.35–26.05, avg. 25.70), affirming a combined crust-mantle lead origin. Both the Xiahulin and Bajiaguan samples plotted in the subduction zone lead range on the Δγ–Δβ diagram (Figure 9), indicating magmatic lead derived from upper crust-mantle mixing.

Hf isotope analysis of syngenetic syenogranite associated with Xiahulin mineralization revealed a primary magma origin primarily from juvenile crustal partial melting derived from mantle,

with minor ancient crustal contamination during its evolution. Similar findings in the Taipingchuan (granodiorite porphyry) and Wunugetushan (monzogranite) copper-molybdenum deposits in the region highlighted mantle-derived young crustal material differentiation, followed by the incorporation of ancient crustal components (Cao, 2020; Zhang et al., 2022).

The trace element composition in rocks and sphalerite represents a certain geochemical significance, and the study of the geochemical characteristics of metallic minerals and mineralized rock bodies is of great significance for the research of the entire deposit. By analyzing the rare earth and trace characteristic parameters of syenogranite and sphalerite in the Xiahulin deposit (Table 2), although the rare earth and trace element characteristics in syenogranite and sphalerite are not consistent, their evolutionary characteristics of rare earth elements, Th/U, Nb, Sr, Zr, Ti and other trace elements indicate a certain degree of inheritance. The higher Th/U values in syenogranite indicate that the magma may

have originated from mantle material, while the weak negative Nb anomaly exhibited by syenogranite to the obvious negative Nb anomaly in sphalerite suggests the involvement of crustal material in the mineralization process (Rollison, 2000). The negative Ti anomaly in syenogranite may indicate the involvement of crustal material in magmatic processes. The rare earth elements in sphalerite are lower than those in syenogranite, but the decrease in heavy rare earth elements is more significant, while the decrease in Eu is not significant. This may be due to the partial melting of plagioclase as a residual phase, which results in a significant decrease in the content of heavy rare earth elements in sphalerite during the gas-liquid and mineralization stages in contact with marble, due to the exchange of a large amount of alkali rich minerals.

The sulfur, lead, zircon Hf isotope trace elements and REE analyses collectively indicated that the metallogenic material source for the Xiahulin lead-zinc deposit was a mixture of crust and mantle components.

6.2 Diagenesis and metallogenic age

According to field observations underground, the lead-zinc mineralization in the Xiahulin deposit is closely related to the skarnization at the contact between syenogranite and marble. In addition, after analysis, there are certain differences in trace elements and rare earth elements between sphalerite and syenogranite, but it can be seen that there is some inheritance (Figure 6). Therefore, we believe that syenogranite should be the ore-forming rock of the Xiahulin lead-zinc deposit. The Rb-Sr isochron age of the sphalerite (191.9 ± 7.9 Ma) (unpublished data) aligned with the zircon LA-ICP-MS age of the syenogranite (203.8 ± 2.2 Ma), indicating Late Triassic to Early Jurassic diagenesis and mineralization. Moreover, a comparative analysis of the geochemical and zircon Hf isotope compositions of the ore-forming syenogranite and regional porphyry copper-molybdenum deposits revealed their coeval formations and shared tectonic settings.

Recent research has provided extensive data on the formation ages of porphyry Cu–Mo deposits in the Erguna Metallogenic Belt. Qin et al. (1999) reported a single-grain zircon U-Pb age of 188.3 ± 0.6 Ma for the ore-bearing monzogranitic porphyry in the Wunugetu deposit, along with an altered sericite K-Ar age of 183.5 ± 1.7 Ma. Li N. et al. (2007) identified a molybdenite Re-Os isochron age of 178 ± 10 Ma, suggesting Early to Middle Jurassic mineralization. In the Taipingchuan deposit, the ore-forming granodiorite porphyry yielded a zircon U-Pb age of 202 ± 5.7 Ma and a molybdenite Re-Os age of around 203 Ma (Chen et al., 2010), indicating Late Triassic mineralization. The quartz diorite porphyry serves as the ore-forming rock of the Baguan deposit, presenting a zircon U-Pb age of 217.6 ± 2.6 Ma and a molybdenite Re-Os model age of 222.4 ± 3.3 Ma. The Erdenet giant porphyry copper-molybdenum deposit in Mongolia records a quartz diorite U-Pb age of 240–246 Ma and a molybdenite Re-Os isochron age of 241 ± 3.1 Ma (Jiang et al., 2010), indicating Middle Triassic diagenesis and mineralization.

The Early Mesozoic porphyry copper-molybdenum and skarn-type lead-zinc mineralization in the Erguna block can be broadly divided into two stages. The first stage, which occurred in the Middle to Late Triassic, included certain deposits, such as the Erdenet

deposit in Mongolia and the Baguan deposit in China. The second stage, spanning from the Late Triassic to Early Jurassic, led to the formation of the Taipingchuan, Wunugetu, and Xiahulin deposits in China. These stages cover approximately 20 Ma and have significant spatial impact on the region.

6.3 Metallogenic dynamic background

Isotopic dating revealed that the Baguan porphyry copper-molybdenum deposit formed in the Late Triassic, while the Taipingchuan copper-molybdenum and Xiahulin lead-zinc deposits developed from the Late Triassic to Early Jurassic. In contrast, the Wunugetu porphyry copper-molybdenum deposit originated in the Early Jurassic. During this period, the Erguna region was located at the intersection of the Paleo-Asian Ocean, Paleo-Pacific, and Mongolia-Okhotsk metallogenic domains. Therefore, understanding the tectonic setting of these copper-molybdenum-lead-zinc deposits is essential for interpreting the region's tectonic evolution.

Tectonic setting discrimination diagrams (Figure 11), based on the lithology of ore-forming rock masses from the Baguan, Taipingchuan, and Xiahulin deposits, illustrate the tectonic evolution of the area, progressing from an intraplate environment to an island arc, then a volcanic arc, and finally a syn-collisional setting. Given that the ore-forming rock masses in this region originated from the upper mantle and were contaminated by crustal materials, they likely formed in an active continental margin setting associated with oceanic crust subduction. Recent geochemical studies of ore-forming rock masses from typical porphyry copper-molybdenum deposits along the Sino-Mongolian border and nearby regions have indicated that these deposits can be formed primarily in an island arc environment owing to oceanic crust subduction (Kuzmin and Antipin, 1993; Xu et al., 1998; Tang et al., 2018; Chen et al., 2010; Zhang et al., 2010).

Emerging evidence suggests that the Paleo-Asian Ocean likely closed during the Middle Triassic (Sun et al., 2004; Li J. et al., 2007; Liu et al., 2011). Although some scholars have proposed that the subduction of the Paleo-Pacific plate toward the Eurasian continent began in the Late Triassic (Peng and Chen, 2007), others argue that the Late Triassic igneous rocks in the eastern Jilin-Heilongjiang region and the Zhangguangcai Range reflect an extensional tectonic setting during this time (Xu et al., 2009; Wu et al., 2011). The presence of Early Jurassic calc-alkaline and bimodal volcanic rock assemblages in the eastern Jilin-Heilongjiang region (Yu et al., 2012; Xu W. et al., 2013; Xu et al., 2013 M., 2019; Tang et al., 2018) suggests that the Paleo-Pacific plate subduction commenced in the Early Jurassic. Therefore, it is evident that the subduction timings of the Paleo-Asian Ocean and Paleo-Pacific Ocean cannot align with the mineralization ages of the copper-molybdenum-lead-zinc deposits in this region.

Most researchers have reported that the Mongolia-Okhotsk Ocean can be a major bay of the Paleo-Asian Ocean with localized subduction, which is closed in a "scissors-like" manner from west to east at the end of the Late Paleozoic due to the rotation of the Siberian Plate relative to the Central Mongolian Block. This closure occurred in stages, with the western segment closing in the Late Triassic and the eastern segment closing in the Late Jurassic

(Zonenshain, 1990; Zorin, 1999; Mo et al., 2005; Mazukabzov et al., 2010). The Erdenet giant porphyry copper-molybdenum deposit in Mongolia, with diagenesis and mineralization ages of approximately 240 Ma (Jiang et al., 2010), formed in a continental marginal arc setting associated with the subduction of this oceanic crust. Lv et al. (2001) proposed that the Mesozoic era in the Manzhouli-Erguna region of China was part of the Mongolia-Okhotsk residual ocean tectonic domain. Recent data have suggested that the Taipingchuan porphyry copper-molybdenum deposit in China's Erguna Block can be formed in the Late Triassic within an active continental margin arc setting, resulting from the subduction of the Mongolia-Okhotsk Ocean beneath the Erguna Block (Chen et al., 2010; Zhang et al., 2010). Wu et al. (2011) also indicated that Early Mesozoic granites in the northern Erguna block were related to the evolution of the Mongolia-Okhotsk Belt.

The above analysis suggests that the Mongolia-Okhotsk oceanic crust experienced bidirectional subduction during the Triassic. The porphyry copper-molybdenum deposits, including Baguan and Taipingchuan, and lead-zinc deposits, such as Xiahulin, in the Erguna block are closely linked to tectono-magmatic processes driven by the subduction of the Mongolia-Okhotsk Ocean. Specifically, during the Late Triassic to Early Jurassic, as the Mongolia-Okhotsk Ocean closed in a "scissors-like" manner, the oceanic crust subducted toward both the Siberian Plate and the Erguna block. Partial melting of lower crustal materials could incorporate minor mantle-derived components and generate granitic magmas enriched in Cu, Mo, Pb, and Zn, exhibiting the characteristics of adakitic and island arc magmatic rocks. This granitic magma, rich in ore-forming elements, ascended through tectonic fractures, forming porphyry bodies such as monzogranitic, quartz diorite, and granodiorite porphyries. As the temperature and pressure decreased and meteoric water mixed in, the ore-forming fluids underwent boiling and immiscibility, precipitating Cu, Mo, and other metals, forming certain deposits such as Baguan, Babayi, Taipingchuan, and Wunugetu. Concurrently, the syenogranitic magma engaged in contact metasomatism with the Ergunahe Formation marble, leading to skarnization. In the middle to late stages of mineralization, further reductions in temperature and pressure and the mixing of meteoric water reduced the solubility of Cu, Pb, and Zn, promoting their enrichment and precipitation, resulting in the lead-zinc deposits such as Xiahulin and Xijinuo Mountain.

7 Conclusion

The mineralization age of the Xiahulin skarn type lead-zinc deposit is (191.9–203.8) Ma, belonging to the Early Cretaceous. This skarn type deposit is consistent with the mineralization age of typical porphyry type copper molybdenum deposits in the study area, which is the product of large-scale mineralization in the Late Triassic Early Cretaceous of the Erguna block.

The ore-forming material source of the Xiahulin lead-zinc deposit is a crust mantle mixed source, which is similar to typical vein shaped lead-zinc deposits and porphyry type copper molybdenum deposits in the area. It is formed by the partial melting of young crust from mantle derived magma, and during the upward migration of magma, skarnization and mineralization processes, accompanied by the addition of crustal and sedimentary

rock materials, they jointly contribute to the formation of mineral materials such as lead and zinc.

In the Triassic, the Mongolia-Okhotsk oceanic crust experienced bidirectional subduction. The porphyry copper-molybdenum deposits, such as Baguan and Taipingchuan, along with skarn-type lead-zinc deposits, such as Xiahulin in the Erguna block, were closely associated with tectono-magmatic processes driven by the subduction of the Mongolia-Okhotsk Ocean.

Data availability statement

The original contributions presented in the study are included in the article/supplementary material, further inquiries can be directed to the corresponding authors.

Author contributions

MD: Conceptualization, Data curation, Investigation, Methodology, Writing–original draft. GC: Conceptualization, Investigation, Project administration, Supervision, Writing–review and editing. TL: Project administration, Supervision, Writing–review and editing. LL: Investigation, Methodology, Writing–review and editing. XZ: Data curation, Investigation, Writing–review and editing.

Conflict of interest

The authors declare that the research was conducted in the absence of any commercial or financial relationships that could be construed as a potential conflict of interest.

Generative AI statement

The author(s) declare that no Generative AI was used in the creation of this manuscript.

Publisher's note

All claims expressed in this article are solely those of the authors and do not necessarily represent those of their affiliated organizations, or those of the publisher, the editors and the reviewers. Any product that may be evaluated in this article, or claim that may be made by its manufacturer, is not guaranteed or endorsed by the publisher.

References

Basuki, N. I., Taylor, B. E., and Spooner, E. T. C. (2008). Sulfur isotope evidence for thermochemical reduction of dissolved sulfate in Mississippi valley-type zinc-lead mineralization, bongara area, northern Peru. *Econ. Geol.* 103, 783–799. doi:10.2113/gsecongeo.103.4.783

Batchelor, R. A., and Bowden, P. (1985). Petrogenetic interpretation of granitoid rock series using multicationic parameters. *Chem. Geol.* 48, 43–55. doi:10.1016/0009-2541(85)90034-8

Boynton, W. V. (1984). Chapter 3 - cosmochemistry of the rare earth elements: meteorite studies. *Dev. Geochem.* 2, 63–114.

Cao, G., Gao, T., and Wu, Y. (2000). Isotope and REE geochemistry of Baoziwan gold deposit, Shanxi, China. *Earth Environ.* 28, 10–15.

Cao, Y. (2020). *Geochemical characteristics and genesis of Mesozoic intrusive rocks in Taipingchuan Mo-Cu deposit, Inner Mongolia*. China. Beijing: China University of Geosciences.

Catchpole, H., Kouzmanov, K., Bendezú, A., Ovtcharova, M., Spikings, R., Stein, H., et al. (2015). Timing of porphyry (Cu-Mo) and base metal (Zn-Pb-Ag-Cu) mineralisation in a magmatic-hydrothermal system—morococha district, Peru. *Miner. Deposita* 50, 895–922. doi:10.1007/s00126-014-0564-x

Chaussidon, M., and Lorand, J.-P. (1990). Sulphur isotope composition of orogenic spinel lherzolite massifs from Ariege (North-Eastern Pyrenees, France): an ion microprobe study. *Geochimica Cosmochimica Acta* 54, 2835–2846. doi:10.1016/0016-7037(90)90018-G

Chen, Z., Zhang, L., Lu, B., Li, Z., Wu, H., Xiang, P., et al. (2010). Geochronology and geochemistry of the Taipingchuan copper-molybdenum deposit in Inner Mongolia, and its geological significances. *Acta Petrol. Sinca* 26, 1437–1449.

Doe, B. R. (1979). "Plumbotectonics: the phanerozoic," in *Geochemistry of hydrothermal ore deposits*, 22–70.

Du, Q. (1988). *Duobaoshan porphyry copper deposit*. Beijing, China: Geology press.

Duan, M., Ren, Y., Xue, C., Yang, Q., Hao, Y., and Liu, T. (2022). Provenance tracing and age analysis of lead-zinc mineralization in Qiyimuchang, Inner Mongolia, NE China. *Minerals* 12, 1146. doi:10.3390/min12091146

Hou, K., Li, Y., and Tian, Y. (2009). *In situ* U-Pb zircon dating using laser ablation-multi ion counting-ICP-MS. *Mineral. deposits* 28, 481–492.

Hou, Z. (2014). *Ore genesis and tectonic setting of Badaguan copper-molybdenum deposit in Erguna region, Inner Mongolia*. Changchun: Jilin University.

Isotope Geology Laboratory of Yichang Institute of Geology and Mineral Resources, Ministry of Geology and Mineral Re-sources (1979). *The basic problem of lead isotope geology*. Beijing: Geological Publishing House, 35–137.

Jahn, B., Windley, B., Natal'in, B., and Dobretsov, N. (2004). Phanerozoic continental growth in central asia. *J. Asian Earth Sci.* 23, 599–603. doi:10.1016/S1367-9120(03)00124-X

Jia, B., Liu, G. X., Zhang, C. H., Yang, H. Z., and Zhang, C. P. (2012). Metallogenesis of the lead-zinc deposits controlled by the Mesozoic volcanic-subvolanic rocks in Daxinganling region. *Geol. Resour.* 21, 114–121.

Jiang, S.-H., Nie, F.-J., Su, Y.-J., Bai, D., and Liu, Y.-F. (2010). Geochronology and origin of the Erdenet superlarge Cu-Mo deposit in Mongolia. *Acta Geosci. Sin.* 31, 289–306.

Kuzmin, M. I., and Antipin, V. S. (1993). Geochemical types of granitoids of the Mongol-Okhotsk belt and their geodynamic settings. *Chin. J. Geochem.* 12, 110–117. doi:10.1007/BF02842192

Li, C. (2009). A review on the mineralogy and situ microanalytical dating techniques of zircons. *Geol. Surv. Res.* 33, 161–174.

Li, J., Gao, L., Sun, G., Li, Y., and Wang, Y. (2007a). Shuangjingzi middle Triassic syn-collisional crust-derived granite in the east Inner Mongolia and its constraint on the timing of collision between Siberian and Sino-Korean paleo-plates. *ACTA PETROL. SIN.* 23, 565–582.

Li, J. W., Liang, Y. W., Wang, X. Y., Zhang, B., Yang, Y. C., She, H. Q., et al. (2011). The origin of the Erdaohezi lead-zinc deposit, Inner Mongolia. *J. Jilin Univ. Sci. Ed.* 41, 1745–1754.

Li, N., Chen, Y., Lai, Y., and Li, W. (2007b). Fluid inclusion study of the Wunugetushan porphyry Cu-Mo deposit, Inner Mongolia. *Acta Petrol. Sin.* 23, 2177–2188.

Li, T. G., Wu, G., Liu, J., Hu, Y. Q., Zhang, Y. F., and Luo, D. F. (2014). Rb-Sr isochron age of the Jiawula Pb-Zn-Ag deposit in the Manzhouli area and its geological significance. *Acta Petrol. Sin.* 30, 257–270.

Li, Y., and Zhao, Y. (2014). Lead isotopes in the sulfide ores from the Shesuo and Lawu copper deposits, northern Xizang. *Sediment. Geol. Tethyan Geol.* 34 (3), 96–105.

Liu, Y., Gao, S., Hu, Z., Gao, C., Zong, K., and Wang, D. (2010). Continental and oceanic crust recycling-induced melt-peridotite interactions in the trans-north China orogen: U-Pb dating, Hf isotopes and trace elements in zircons from mantle xenoliths. *J. Petrology* 51, 537–571. doi:10.1093/petrology/egp082

Liu, Y., Zhang, X., Chi, X., Wen, Q., Chen, Y., Han, G., et al. (2011). Deformation and tectonic layer division of the upper paleozoic in daxing'anling area. Journal of Jilin university. *Earth Sci. Ed.* 41, 1304–1313.

Lu, Y. (2004). GeoKit——a geochemical toolkit for microsoft excel. *Geochimica* 33, 459–464.

Lv, S., Lu, B., Zhao, W., and Zhang, Y. (2023). Simultaneous determination of 23 major, minor and trace components in soil and stream sediment by X-Ray fluorescence spectrometry. *PTCA(Part B CHEM.ANAL.)* 59 (7), 764–770.

Lv, Z., Duan, G., Hao, L., Li, D., and Dong, G. (2001). The interaction system between mesozoic tectonics, fluids, petrogenesis and mineralization in the northeast of the Northern Orogenic Belt, China. *Geotect. Metsllagenia* 25, 161–170.

Maniar, P. D., and Piccoli, P. M. (1989). Tectonic discrimination of granitoids. *Geol. Soc. Am. Bull.* 101, 635–643. doi:10.1130/0016-7606(1989)101<0635:TDOG>2.3.CO;2

Mao, J. W., Xie, G. Q., Zhang, Z. H., Li, X. F., Wang, Y. T., Zhang, C. Q., et al. (2005). Mesozoic large-scale metallogenic pulses in North China and corresponding geodynamic settings. *Acta Petrol. Sin.* 21, 169–188.

Mazukabzov, A. M., Donskaya, T. V., Gladkochub, D. P., and Paderin, I. P. (2010). The late paleozoic geodynamics of the west transbaikalian segment of the central asian fold belt. *Russ. Geol. Geophys.* 51, 482–491. doi:10.1016/j.rgg.2010.04.008

Middlemost, E. A. K. (1972). A simple classification of volcanic rocks. *Bull. Volcanol.* 36, 382–397. doi:10.1007/BF02596878

Mo, S., Han, M., and Li, J. (2005). Compositions and orogenic processes of Mongolia-Okhotsk orogen. *J. Shandong Univ. Sci. Technol. Nat. Sci.* 24, 50–52.

Pan, P., Xiao, Q., Lu, S., Deng, J., Feng, Y., Zhang, K., et al. (2009). Subdivision of tectonic units in China. *Geol. China* 36, 1–4.

Pearce, J. A., Harris, N. B. W., and Tindle, A. G. (1984). Trace element discrimination diagrams for the tectonic interpretation of granitic rocks. *J. Petrology* 25, 956–983. doi:10.1093/petrology/25.4.956

Peccerillo, A., and Taylor, S. R. (1976). Geochemistry of eocene calc-alkaline volcanic rocks from the Kastamonu area, Northern Turkey. *Contr. Mineral. Petrol.* 58, 63–81. doi:10.1007/BF00384745

Peng, Y., and Chen, Y. (2007). Location of the tectonic boundary between the jilin-heilongjiang orogenic belt and the kaiyuan shancheng section of the north China platform. *Globle Geol.* 26, 1–6.

Pirajno, F. (2009). *Hydrothermal processes and mineral systems*. Berlin, Germany: Springer.

Qin, K., Li, H., Li, W., and Ishihara, S. (1999). Intrusion and mineralization ages of the Wunugetushan porphyry Cu–Mo deposit, Inner Mongolia, northwestern China. *Geol. Rev.* 45, 180–185.

Rollison, H. R. (2000). *Petrogeochemistry[M]. Translate by yang X M, yang X Y, chen S X*. Hefei: China University of science and Technology Press, 40–112.

Sláma, J., Košler, J., Condon, D. J., Crowley, J. L., Gerdes, A., Hanchar, J. M., et al. (2008). Plešovice zircon—a new natural reference material for U–Pb and Hf isotopic microanalysis. *Chem. Geol.* 249, 1–35. doi:10.1016/j.chemgeo.2007.11.005

Sun, D., Wu, F., Zhang, Y., and Gao, S. (2004). The final closing time of the west Lamulun River-Changchun-Yanji plate suture zone: evidence from the Dayushan granitic pluton, Jilin Province. *J. Jilin Univ. Earth Sci. Ed.* 34, 174–181.

Sun, E. S. (1995). The metallogenic regularity of the silver deposits in the Manzhouli-Xinbaerhuyouqi metallogenic belt, Inner Mongolia. *Geol. Explor. non-ferrous Metals* 4, 23–29.

Sun, S.-s., and McDonough, W. F. (1989). Chemical and isotopic systematics of oceanic basalts: implications for mantle composition and processes. *SP* 42, 313–345. doi:10.1144/GSL.SP.1989.042.01.19

Tan, G. (2011). *The ore-forming processes and mineralization of Wunugetushan porphyry Cu–Mo deposit*. Inner Mongolia. Beijing: Chinese Academy of Geological Sciences.

Tang, J., Xu, W., Wang, F., and Ge, W. (2018). Subduction history of the paleo-pacific slab beneath eurasian continent:mesozoic-paleogene magmatic records in northeast asia. *Sci. China Earth Sci.* 61, 527–559. doi:10.1007/s11430-017-9174-1

Tang, W., Li, J., and Wang, G. (2018). Geochemical features of the typical porphyry copper deposits in China- Mongolia border and its neighbor areas. *Geol. Surv. Res.* 33, 98–104.

Wang, H., Wang, L., and Guan, W. (2003). *Verification report on resource reserves of lead zinc silver ore bodies I and II in Xiahulin deposit*. Erguna City, Inner Mongolia, China: National geological data center of China.

Wilson, B. M. (1989). *Igneous petrogenesis:A global tectonic approach*. Springer London, Limited: Guildford, Berlin.

Wu, F.-Y., Sun, D.-Y., Ge, W.-C., Zhang, Y.-B., Grant, M. L., Wilde, S. A., et al. (2011). Geochronology of the Phanerozoic granitoids in northeastern China. *J. Asian Earth Sci.* 41, 1–30. doi:10.1016/j.jseaes.2010.11.014

Wu, Y., and Zheng, Y. (2004). Genesis of zircon and its constraints on interpretation of U-Pb age. *Chin. Sci. Bull.* 49, 1554–1569. doi:10.1007/BF03184122

Xiang, W., Hu, S., Yan, H., and Lian, C. (1998). Main characteristics of Ag-Pb-Zn deposits and discussion on their mineralization on the western slope of the Great Hinggan Moutains, NE, China and neighbouring area. *Uranium Geol.* 14 (6), 344–351.

Xu, G., Bian, Q., and Wang, Y. (1998). Tectonic evolution and metallization of the Erguna orogenic belt. *Chin. J. Geol.* 33, 84–92.

Xu, G., Xie, W., and Han, W. (2017). *Detailed investigation report on lead zinc silver mine production in Xiahulin deposit*. Erguna City, Inner Mongolia, China: National geological data center of China.

Xu, M., Xu, W., Wang, F., Gao, F., and Yu, J. (2013a). Geochronology and geochemistry of the early jurassic granitoids in the central lesser xing' an range, NE China and its tectonic implications. *ACTA PETROL. SIN.* 29, 354–368.

Xu, W., Sun, C., Tang, J., Luan, J., and Wang, F. (2019). Basement nature and tectonic evolution of the xing'an-Mongolian orogenic belt. *Earth Sci. - J. China Univ. Geosciences* 44, 1620–1646.

Xu, W., Wang, F., Pei, F., Meng, E., Tang, J., Xu, M., et al. (2013b). Mesozoic tectonic regimes and regional ore-forming background in NE China: constraints from spatial and temporal variations of Mesozoic volcanic rock associations. *ACTA PETROL. SIN.* 29, 339–353.

Xu, W.-L., Ji, W.-Q., Pei, F.-P., Meng, E., Yu, Y., Yang, D.-B., et al. (2009). Triassic volcanism in eastern Heilongjiang and Jilin provinces, NE China: chronology, geochemistry, and tectonic implications. *J. Asian Earth Sci.* 34, 392–402. doi:10.1016/j.jseaes.2008.07.001

Xu, Z. T. (2020). *Ore genesis and geodynamic background of lead-zinc polymetallic deposits in Erguna area, inner Mongolia*. Changchun: Jilin University.

Yang, B., Chen, Z., Zhang, Q., Zhou, Z., Han, F., Zhang, W., et al. (2018). Geological characteristics and sulfur and lead isotopes of the Kanling lead-zinc deposit, Southern Tianshan Mountains. *Geol. China* 45, 155–167.

Yu, J.-J., Wang, F., Xu, W.-L., Gao, F.-H., and Pei, F.-P. (2012). Early Jurassic mafic magmatism in the Lesser Xing'an–Zhangguangcai Range, NE China, and its tectonic implications: constraints from zircon U–Pb chronology and geochemistry. *Lithos* 142–143, 256–266. doi:10.1016/j.lithos.2012.03.016

Zartman, R. E., and Doe, B. R. (1981). Plumbotectonics—the model. *Tectonophysics* 75, 135–162. doi:10.1016/0040-1951(81)90213-4

Zhai, D., Liu, J., Wang, J., Yao, M., Liu, X., Liu, Z., et al. (2013). A study of stable isotope geochemistry of the Jiawula large Pb–Zn–Ag ore deposit, Inner Mongolia. *Earth Sci. Front.* 20, 213–225.

Zhang, B. (2011). *The geological features and genesis of the Dongjun lead-zinc-silver deposit in Inner Mongolia*. Beijing China : Chinese Academy of Geological Sciences.

Zhang, J. F., Wang, X. Z., Quan, H., Wu, G., and Zhu, H. C. (2002). The forming conditions of nonferrous and precious metal deposits in the north of Derbugan metallogenic province. *Geol. Resour.* 11, 43–52.

Zhang, L., Chen, Z., Wu, H., Xiang, P., and Huang, S. (2010). The tectonic magmatic mineralization and dynamic background of the Delbugan polymetallic mineralization belt in the Mongolian Okhotsk orogenic belt. *Mineral. deposits* 29, 125–126.

Zhang, W., Hu, Z., Günther, D., Liu, Y., Ling, W., Zong, K., et al. (2016). Direct lead isotope analysis in Hg-rich sulfides by LA-MC-ICP-MS with a gas exchange device and matrix-matched calibration. *Anal. Chim. Acta* 948, 9–18. doi:10.1016/j.aca.2016.10.040

Zhang, W., Hu, Z., and Liu, Y. (2020). Iso-Compass: new freeware software for isotopic data reduction of LA-MC-ICP-MS. *J. Anal. At. Spectrom.* 35, 1087–1096. doi:10.1039/D0JA00084A

Zhang, X., Zhang, Y., Liu, K., He, X., Wang, S., Jia, W., et al. (2022). Zircon U-Pb and Lu-Hf isotopic dating of magmatic rocks in the Wunugetushan porphyry copper-molybdenum deposit, Inner Mongolia. *Rock Mineral Analysis* 41, 774–788.

Zhao, W., Zhang, T., Lu, B., Zhou, C., and Zhang, Y. (2021). Study on determination of rare earth elements in geological samples by ICP-MS and WD-XRF. *Mod. Chem. Ind.* 41 (3), 0244–0250.

Zhao, Y., Lv, J. C., Zhang, D. B., Zhou, Y. H., Shao, J., and Wang, B. (2017). Rb-Sr isochron age of Derbur Pb-Zn-Ag deposit in Erguna massif of northeast Inner Mongolia and its geological significance. *Mineral. Deposits* 36, 893–904.

Zhu, B., Li, S., Dai, T., Chen, Y., Fan, S., Gui, X., et al. (1998). "Isotopes system theory and its application," in *Earth science-on the evolution of the continental crust and mantle* (Beijing: Science Press).

Zhu, H. C., Zhang, J. F., Quan, H., Zhang, H., and Wang, H. B. (1999). Metallogenic characteristics of nonferrous and noble metals in Ergun region. *J. Precious Metallic Geol.* 8, 193–198.

Zonenshain, L. P. (1990). *Geology of the ussr: a plate-tectonic synthesis (geodynamics series)*. 1st ed. Washington DC: American Geophysical Union.

Zorin, Yu. A. (1999). Geodynamics of the western part of the Mongolia–Okhotsk collisional belt, Trans-Baikal region (Russia) and Mongolia. *Tectonophysics* 306, 33–56. doi:10.1016/S0040-1951(99)00042-6